Constitutive equations for a polymer fluid based on the concept of non-affine networks

A.D. Drozdov* and R.K. Gupta

Department of Chemical Engineering

West Virginia University

P.O. Box 6102

Morgantown, WV 26506, USA

Abstract

Constitutive equations are developed for a polymer fluid, which is treated as a permanent network of strands bridged by junctions. The junctions are assumed to slide with respect to their reference positions under loading. Governing equations are derived by using the laws of thermodynamics under the assumption that the vorticity tensor for the flow of junctions is proportional to that for macro-deformation. Explicit expressions are developed for the steady elongational viscosity, as well as for the steady shear viscosity and normal stress functions. To verify the constitutive relations, three sets of experimental data are approximated on polystyrene solutions with various molecular weights. It is demonstrated that the model can correctly describe stress overshoot for the shear stress and first normal stress difference in start-up tests with various strain rates. Adjustable parameters in the governing equations change consistently with the strain rate, molecular weight and concentration of entanglements. To validate the constitutive equations, observations on low-density polyethylene melt in uniaxial extensional flow are compared with the results of numerical analysis when the material constants are found by matching experimental data in shear tests.

Key-words: Polymer fluid, Non-affine network, Stress overshoot, Constitutive equations, Finite deformations

1 Introduction

This paper is concerned with modelling the rate-dependent response of polymer fluids at finite strains. In particular, the present study focuses on constitutive equations that can adequately describe stress overshoot under shear. The latter phenomenon has attracted substantial attention in the past three decades, because it provides a severe test for the analysis of rheological models.

---

*Corresponding author. Fax: (304) 293 4139; E-mail: Aleksey.Drozdov@mail.wvu.edu

Experimental studies demonstrate that under shear flow with a constant strain rate at isothermal conditions, the shear stress and the first normal stress difference grow monotonically with time to their ultimate values when the shear rate is relatively small. With an increase in the strain rate, the dependence of the shear stress on time becomes non-monotonic: it reaches a maximum at some instant (overshoot) and decreases to its limiting value afterwards (strain softening). At sufficiently high shear rates, the dependencies of both the shear stress and the first normal stress difference on time becomes non-monotonic, but the time when the first normal stress difference reaches its maximum noticeably exceeds that for the shear stress. The instants when the shear stress and the first normal stress difference become maximal are strongly affected by strain rate: the higher the shear rate is, the earlier the overshoots occur and the larger are the maximal stresses.

Stress overshoot has been observed in conventional shear tests on polymer melts [1, 2, 3, 4, 5, 6], immiscible molten blends of polymers [7], polymer melts filled with micro- [8] and nano-particles [9, 10], polymer solutions [11, 12, 13], solutions of associative copolymers [14], surfactant solutions [15], solutions of wormlike micelles [16, 17], liquid crystalline polymers [18] and discotic mesophases [19], bicontinuous microemulsions [20], colloidal suspensions [21, 22], and suspensions of rod-like macromolecules [23], to mention a few. This list demonstrates that stress overshoot is a rather common phenomenon observed in complex fluids. Comparison of experimental data for polymer solutions and melts with results of numerical simulation reveals that several constitutive equations can qualitatively describe stress overshoot under shear. We would mention among them the single integral model [2], the Giesekus model [24], the concept of temporary networks [25], the finitely extensible nonlinear elastic (FENE) network model [26], the reptation concept that incorporates segmental stretching [11, 27], and the pom–pom model [28, 29].

However, even the most sophisticated constitutive equations that include a number of adjustable parameters can reproduce observations for the shear stress and the first normal stress difference in start-up shear tests only qualitatively, and, when their parameters are fitted to describe the stress overshoot, they fail to adequately predict the steady shear viscosity (see Figure 12 in [29]). This observation may be explained by the fact that physical reasons for the origin of stress overshoot remain rather obscure, and not all of them are taken into account in conventional models. The following possible mechanisms for the onset of stress overshoot are mentioned: (i) changes in the concentration of entanglements and entanglement spacing [14], (ii) changes in the orientation of polymer coils [30] and nonuniform segmental stretching [30], (iii) formation of an anisotropic mechanically-induced mesoscopic structure [9] that becomes unstable at relatively high strain rates [16], and (iv) reorientation of meso-domains toward a steady-state aligned flow [18, 19].

Although it is conventionally accepted that ordering of strands and their reorientation driven by shear flow provide the most important mechanism for stress overshoot and subsequent strain softening, to the best of our knowledge, no attempts have been made to incorporate this phenomenon into constitutive equations explicitly and to assess the effect of molecular structure of a polymer on the kinetics of reorientation. An important point here is that at finite strains, the evolution of an infinitesimal volume that can rotate with respect to macro-deformations is determined by two tensors: a symmetric rate-of-strain tensor and a skew-symmetric vorticity tensor (the so-called plastic spin), while the latter is conventionally disregarded in constitutive models for polymer fluids (despite the observation that "it is the

2

vorticity in shearing that leads to its extreme strain softening" [31]).

The objective of this study is two-fold: (i) to develop constitutive equations for the response of polymer fluids that account for the evolution of the plastic spin, on the one hand, and that involve a relatively small number of material constants, on the other, and (ii) to demonstrate that these relations describe stress overshoot under shear of polymer solutions and melts quantitatively, while their adjustable parameters change consistently with strain rate and molecular structure of polymer fluids.

A polymer fluid is treated as a network of chains bridged by junctions (entanglements and physical cross-links whose life-time exceeds the characteristic time of an experiment). The network is assumed to move non-affinely: the junctions between strands can slide with respect to their reference positions in the bulk material under deformation. Following [32], we suppose that the vorticity tensor for viscoplastic flow of junctions is proportional to that for macro-deformation, whereas the rate-of-strain tensor for sliding of junctions is determined by the laws of thermodynamics. To simplify the analysis, we disregard rearrangement of strands in the network (which implies that we confine ourselves to relatively slow motions whose characteristic time exceeds the characteristic time for relaxation of stresses). This allows constitutive equations to be derived which describe any set of observations for the shear stress and the first normal stress difference in start-up shear tests by only four constants that have a transparent physical meaning. These parameters are found by matching experimental data for monodisperse polystyrene (PS) solutions with various mass-average molecular weights and molecular weights between entanglements and for a melt of low-density polyethylene (LDPE).

The exposition is organized as follows. Basic kinematic relations for a non-affine network are derived in Section 2. Constitutive equations for a polymer fluid are developed in Section 3, where it is demonstrated that these relations generalize some well-known rheological models (Johnson–Segalman model [32], Phan-Thien–Tanner model [33], Giesekus model [24], and Leonov model [34]). Phenomenological relations for adjustable functions in the governing equations are suggested in Section 4. The governing relations are simplified for uniaxial extension in Section 5 and simple shear in Section 6, where explicit formulas are developed for the steady elongational and shear viscosities. In Section 7, material constants are found by fitting observations in start-up shear tests. A discussion of the effects of shear rate and molecular weight distribution on these quantities is provided in Section 8. The model is validated in Section 9 by comparison of results of numerical simulation for LDPE melt in extensional and shear flows. Some concluding remarks are formulated in Section 10.

2 Kinematic relations

With reference to the concept of non-affine networks, a polymer fluid is modelled as a network of strands bridged by junctions that can slide with respect to their reference positions under deformation. Denote by $\mathbf{F}(t)$ the deformation gradient for transition from the initial state to the actual state at time $t \geq 0$, and by $\mathbf{F}_s(t)$ the deformation gradient for transition from the initial state to the reference state associated with sliding of junctions. It is presumed that the transformations described by the tensors $\mathbf{F}(t)$ and $\mathbf{F}_s(t)$ are volume-preserving, which means that the third principal invariants of these tensors equal unity.

3

The elastic deformation gradient $\mathbf{F}_e(t)$ [the deformation gradient for transition from the current reference state for junctions (the so-called intermediate state) to the actual state of the network] is determined by the conventional formula for the multiplicative decomposition of the deformation gradient

$$\mathbf{F}_e(t) = \mathbf{F}(t) \cdot \mathbf{F}_s^{-1}(t), \tag{1}$$

where the dot stands for inner product. Differentiation of Eq. (1) with respect to time t implies that

$$\frac{d\mathbf{F}_e}{dt}(t) = \mathbf{L}(t) \cdot \mathbf{F}_e(t) - \mathbf{F}(t) \cdot \mathbf{F}_s^{-1}(t) \cdot \frac{d\mathbf{F}_s}{dt}(t) \cdot \mathbf{F}_s^{-1}(t), \tag{2}$$

where

$$\mathbf{L}(t) = \frac{d\mathbf{F}}{dt}(t) \cdot \mathbf{F}^{-1}(t) \tag{3}$$

is the velocity gradient. Using Eq. (1) and introducing the elastic velocity gradient $\mathbf{L}_e(t)$ and the velocity gradient for sliding of junctions $\mathbf{l}_s(t)$ by the formulas analogous to Eq. (3),

$$\mathbf{L}_e(t) = \frac{d\mathbf{F}_e}{dt}(t) \cdot \mathbf{F}_e^{-1}(t), \qquad \mathbf{l}_s(t) = \frac{d\mathbf{F}_s}{dt}(t) \cdot \mathbf{F}_s^{-1}(t), \tag{4}$$

we present Eq. (2) in the form

$$\mathbf{L}_e(t) = \mathbf{L}(t) - \mathbf{F}_e(t) \cdot \mathbf{l}_s(t) \cdot \mathbf{F}_e^{-1}(t). \tag{5}$$

Setting

$$\mathbf{L}_s(t) = \mathbf{F}_e(t) \cdot \mathbf{l}_s(t) \cdot \mathbf{F}_e^{-1}(t) \tag{6}$$

in Eq. (5), we arrive at the additive decomposition of the velocity gradients

$$\mathbf{L}_e(t) = \mathbf{L}(t) - \mathbf{L}_s(t). \tag{7}$$

The left and right Cauchy–Green tensors for elastic deformation are given by

$$\mathbf{B}_e(t) = \mathbf{F}_e(t) \cdot \mathbf{F}_e^\top(t), \qquad \mathbf{C}_e(t) = \mathbf{F}_e^\top(t) \cdot \mathbf{F}_e(t), \tag{8}$$

where $\top$ denotes transpose. We differentiate the first equality in Eqs. (8) with respect to time, use Eqs. (4) and (7), and find that

$$\frac{d\mathbf{B}_e}{dt}(t) = \left[\mathbf{L}(t) \cdot \mathbf{B}_e(t) + \mathbf{B}_e(t) \cdot \mathbf{L}^\top(t)\right] - \left[\mathbf{L}_s(t) \cdot \mathbf{B}_e(t) + \mathbf{B}_e(t) \cdot \mathbf{L}_s^\top(t)\right]. \tag{9}$$

Differentiation of the other equality in Eqs. (8) results in

$$\frac{d\mathbf{C}_e}{dt}(t) = 2\mathbf{F}_e^\top(t) \cdot \mathbf{D}_e(t) \cdot \mathbf{F}_e(t), \tag{10}$$

where

$$\mathbf{D}_e(t) = \frac{1}{2}\left[\mathbf{L}_e(t) + \mathbf{L}_e^\top(t)\right]$$

is the rate-of-strain tensor for elastic deformation. It follows from Eqs. (8) and (10) that

$$\frac{d\mathbf{C}_e^{-1}}{dt}(t) = -2\mathbf{F}_e^{-1}(t) \cdot \mathbf{D}_e(t) \cdot \mathbf{F}_e^{-\top}(t). \tag{11}$$

4

For volume-preserving deformations, the first and second principal invariants of the right Cauchy–Green tensor $\mathbf{C}_e(t)$ read

$$J_{e1}(t) = \mathcal{I}_1\big(\mathbf{C}_e(t)\big) = \mathbf{C}_e(t) : \mathbf{I}, \qquad J_{e2}(t) = \mathcal{I}_1\big(\mathbf{C}_e^{-1}(t)\big) = \mathbf{C}_e^{-1}(t) : \mathbf{I}. \tag{12}$$

where $\mathcal{I}_1$ denotes the first invariant of a tensor, $\mathbf{I}$ is the unit tensor, and the colon stands for convolution. Differentiating the first equality in Eqs. (12) with respect to time and using Eqs. (8) and (10), we obtain

$$\frac{dJ_{e1}}{dt}(t) = 2\mathbf{B}_e(t) : \mathbf{D}_e(t). \tag{13}$$

Differentiation of the other equality in Eqs. (12) together with Eqs. (8) and (11) results in

$$\frac{dJ_{e2}}{dt}(t) = -2\mathbf{B}_e^{-1}(t) : \mathbf{D}_e(t). \tag{14}$$

Equations (13) and (14) imply that the derivative of an arbitrary smooth function $\Phi(J_{e1}, J_{e2})$ of the first two principal invariants of the right Cauchy–Green tensor for elastic deformation $\mathbf{C}_e(t)$ with respect to time t is given by

$$\frac{d\Phi}{dt}\big(J_{e1}(t), J_{e2}(t)\big) = 2\big[\Phi_1(t)\mathbf{B}_e(t) - \Phi_2(t)\mathbf{B}_e^{-1}(t)\big] : \mathbf{D}_e(t), \tag{15}$$

where

$$\Phi_m(t) = \frac{\partial \Phi}{\partial J_{em}}\big(J_{e1}(t), J_{e2}(t)\big) \qquad (m = 1, 2).$$

It follows from Eq. (7) that

$$\mathbf{D}_e(t) = \mathbf{D}(t) - \mathbf{D}_s(t), \tag{16}$$

where

$$\mathbf{D}(t) = \frac{1}{2}\big[\mathbf{L}(t) + \mathbf{L}^\top(t)\big], \qquad \mathbf{D}_s(t) = \frac{1}{2}\big[\mathbf{L}_s(t) + \mathbf{L}_s^\top(t)\big]$$

are the rate-of-strain tensors for macro-deformation and sliding of junctions, respectively. Combining Eqs. (15) and (16), we find that

$$\begin{aligned}
\frac{d\Phi}{dt}\big(J_{e1}(t), J_{e2}(t)\big) &= 2\Big\{\big[\Phi_1(t)\mathbf{B}_e(t) - \Phi_2(t)\mathbf{B}_e^{-1}(t)\big] : \mathbf{D}(t) \\
&\quad - \big[\Phi_1(t)\mathbf{B}_e(t) - \Phi_2(t)\mathbf{B}_e^{-1}(t)\big] : \mathbf{D}_s(t)\Big\}.
\end{aligned} \tag{17}$$

It is convenient to present the velocity gradients $\mathbf{L}(t)$ and $\mathbf{L}_s(t)$ as the sums of the rate-of-strain tensors and vorticity tensors,

$$\mathbf{L}(t) = \mathbf{D}(t) + \boldsymbol{\Omega}(t), \qquad \mathbf{L}_s(t) = \mathbf{D}_s(t) + \boldsymbol{\Omega}_s(t), \tag{18}$$

where

$$\boldsymbol{\Omega}(t) = \frac{1}{2}\big[\mathbf{L}(t) - \mathbf{L}^\top(t)\big], \qquad \boldsymbol{\Omega}_s(t) = \frac{1}{2}\big[\mathbf{L}_s(t) - \mathbf{L}_s^\top(t)\big].$$

Without loss of generality, we present the rate-of-strain tensor $\mathbf{D}_s(t)$ in the form

$$\mathbf{D}_s(t) = \beta(t)\mathbf{D}(t) + \mathbf{M}(t), \tag{19}$$

5

where $\beta(t)$ is a non-negative scalar function and

$$\mathbf{M}(t) = \mathbf{D}_s(t) - \beta(t)\mathbf{D}(t). \tag{20}$$

Substitution of expression (19) into Eq. (17) implies that

$$\begin{aligned}
\frac{d\Phi}{dt}\Big(J_{e1}(t), J_{e2}(t)\Big) &= 2\Big\{\Big(1-\beta(t)\Big)\Big[\Phi_1(t)\mathbf{B}_e(t) - \Phi_2(t)\mathbf{B}_e^{-1}(t)\Big]' : \mathbf{D}(t) \\
&\quad - \Big[\Phi_1(t)\mathbf{B}_e(t) - \Phi_2(t)\mathbf{B}_e^{-1}(t)\Big]' : \mathbf{M}(t)\Big\},
\end{aligned} \tag{21}$$

where the prime stands for the deviatoric component of a tensor and we bear in mind that the tensors $\mathbf{D}(t)$ and $\mathbf{M}(t)$ are traceless. Following [32], we assume the vorticity tensor for sliding of junctions to be proportional to the vorticity tensor for macro-deformation

$$\mathbf{\Omega}_s(t) = \gamma(t)\mathbf{\Omega}(t), \tag{22}$$

where $\gamma(t)$ is a non-negative scalar function. Equations (18), (19) and (22) result in

$$\mathbf{L}_s(t) = \mathbf{M}(t) + \beta(t)\mathbf{D}(t) + \gamma(t)\mathbf{\Omega}(t). \tag{23}$$

Combining Eqs. (9) and (22), we arrive at the differential equation for the left Cauchy–Green tensor for elastic deformation

$$\begin{aligned}
\frac{d\mathbf{B}_e}{dt}(t) &= \Big[\mathbf{L}(t) \cdot \mathbf{B}_e(t) + \mathbf{B}_e(t) \cdot \mathbf{L}^\top(t)\Big] - \beta(t)\Big[\mathbf{D}(t) \cdot \mathbf{B}_e(t) + \mathbf{B}_e(t) \cdot \mathbf{D}(t)\Big] \\
&\quad - \Big[\mathbf{M}(t) \cdot \mathbf{B}_e(t) + \mathbf{B}_e(t) \cdot \mathbf{M}(t)\Big] - \gamma(t)\Big[\mathbf{\Omega}(t) \cdot \mathbf{B}_e(t) - \mathbf{B}_e(t) \cdot \mathbf{\Omega}(t)\Big],
\end{aligned}$$

where we take into account that $\mathbf{M}(t)$ is a symmetric tensor and $\mathbf{\Omega}(t)$ is a skew-symmetric tensor. Excluding the vorticity tensor $\mathbf{\Omega}(t)$ by means of Eq. (18), we obtain

$$\begin{aligned}
\frac{d\mathbf{B}_e}{dt}(t) &= \Big(1-\gamma(t)\Big)\Big[\mathbf{L}(t) \cdot \mathbf{B}_e(t) + \mathbf{B}_e(t) \cdot \mathbf{L}^\top(t)\Big] \\
&\quad + \Big(\gamma(t) - \beta(t)\Big)\Big[\mathbf{D}(t) \cdot \mathbf{B}_e(t) + \mathbf{B}_e(t) \cdot \mathbf{D}(t)\Big] \\
&\quad - \Big[\mathbf{M}(t) \cdot \mathbf{B}_e(t) + \mathbf{B}_e(t) \cdot \mathbf{M}(t)\Big].
\end{aligned} \tag{24}$$

Our aim now is to apply Eqs. (21) and (24) to derive constitutive equations for a polymer fluid by using the laws of thermodynamics.

3   Constitutive equations

Denote by N the average number of strands per unit volume of a network and by w the average strain energy per strand. For an isotropic incompressible network, the quantity w is treated as a function of the first two principal invariants of the right Cauchy–Green tensor, $w = w\Big(J_{e1}(t), J_{e2}(t)\Big)$. Neglecting the energy of interaction between strands (this energy is accounted for by means of the incompressibility condition [25]), we define the strain energy per unit volume as the sum of the strain energies of strands,

$$W = Nw. \tag{25}$$

6

For isothermal deformation of an incompressible medium at a reference temperature Θ_0, the Clausius–Duhem inequality reads

$$Q(t) = -\frac{dW}{dt}(t) + \mathbf{\Sigma}'(t) : \mathbf{D}(t) \geq 0,$$

where Q is internal dissipation per unit volume, and $\mathbf{\Sigma}$ is the Cauchy stress tensor. Substituting expression (25) into this formula and using Eq. (21), we find that

$$
\begin{aligned}
Q(t) &= -2N\bigg\{\big(1 - \beta(t)\big)\big[w_1(t)\mathbf{B}_{\mathrm{e}}(t) - w_2(t)\mathbf{B}_{\mathrm{e}}^{-1}(t)\big]' : \mathbf{D}(t) \\
&\quad - \big[w_1(t)\mathbf{B}_{\mathrm{e}}(t) - w_2(t)\mathbf{B}_{\mathrm{e}}^{-1}(t)\big]' : \mathbf{M}(t)\bigg\} + \mathbf{\Sigma}'(t) : \mathbf{D}(t) \geq 0,
\end{aligned}
\tag{26}
$$

where the functions $w_m(t)$ are given by

$$w_m(t) = \frac{\partial w}{\partial J_{\mathrm{e}m}}\big(J_{\mathrm{e}1}(t), J_{\mathrm{e}2}(t)\big) \qquad (m = 1, 2). \tag{27}$$

The dissipation inequality (26) is satisfied for an arbitrary deformation program, provided that the stress tensor reads

$$\mathbf{\Sigma}(t) = -P(t)\mathbf{I} + 2N\big(1 - \beta(t)\big)\big[w_1(t)\mathbf{B}_{\mathrm{e}}(t) - w_2(t)\mathbf{B}_{\mathrm{e}}^{-1}(t)\big], \tag{28}$$

and the tensor $\mathbf{M}(t)$ is given by

$$\mathbf{M}(t) = \alpha(t)\big[w_1(t)\mathbf{B}_{\mathrm{e}}(t) - w_2(t)\mathbf{B}_{\mathrm{e}}^{-1}(t)\big]'. \tag{29}$$

Here $P(t)$ is an unknown pressure, and $\alpha(t)$ is a non-negative scalar function.

It follows from Eqs. (12) and (29) that

$$\mathbf{M} \cdot \mathbf{B}_{\mathrm{e}} + \mathbf{B}_{\mathrm{e}} \cdot \mathbf{M} = 2\alpha\bigg[w_1\bigg(\mathbf{B}_{\mathrm{e}}^2 - \frac{1}{3}J_{\mathrm{e}1}\mathbf{B}_{\mathrm{e}}\bigg) - w_2\bigg(\mathbf{I} - \frac{1}{3}J_{\mathrm{e}2}\mathbf{B}_{\mathrm{e}}\bigg)\bigg].$$

Substitution of this expression into Eq. (24) results in the kinetic equation

$$
\begin{aligned}
\frac{d\mathbf{B}_{\mathrm{e}}}{dt}(t) &= \big(1 - \gamma(t)\big)\big[\mathbf{L}(t) \cdot \mathbf{B}_{\mathrm{e}}(t) + \mathbf{B}_{\mathrm{e}}(t) \cdot \mathbf{L}^{\top}(t)\big] \\
&\quad + \big(\gamma(t) - \beta(t)\big)\big[\mathbf{D}(t) \cdot \mathbf{B}_{\mathrm{e}}(t) + \mathbf{B}_{\mathrm{e}}(t) \cdot \mathbf{D}(t)\big] \\
&\quad - 2\alpha(t)\bigg[w_1(t)\mathbf{B}_{\mathrm{e}}^2(t) + \frac{1}{3}\big(w_2(t)J_{\mathrm{e}2}(t) - w_1(t)J_{\mathrm{e}1}(t)\big)\mathbf{B}_{\mathrm{e}}(t) - w_2(t)\mathbf{I}\bigg].
\end{aligned}
\tag{30}
$$

Given a deformation program, Eqs. (28) and (30) provide a set of constitutive equations that involve four functions to be determined: the strain energy per strand $w(J_{\mathrm{e}1}, J_{\mathrm{e}2})$, the function $\alpha(t)$ that characterizes the rate of internal dissipation, and the functions $\beta(t)$ and $\gamma(t)$ that establish connections between the rate-of-strain tensors and vorticity tensors for sliding of junctions and macro-deformation, respectively. It is worth noting that Eqs. (28) and (30) are applicable for the description of the mechanical response of both solid polymers and polymer fluids, because no assumptions were introduced in their derivation regarding the specific properties of a network of strands.

An important feature of polymer fluids is that their time-dependent behavior reflects two different mechanisms at the micro-level: (i) sliding of junctions between chains with respect to their reference positions, and (ii) slippage of chains with respect to entanglements. Two approaches are conventionally employed to take into account the latter process (which is not included into the present model).

According to the first (the concept of transient networks [25]), it is assumed that strands are not permanently connected to their junctions, but detach from the junctions at random instants, see Figure 1 in [25]. When an end of an active strand separates from a junction, the strand is transformed into the dangling state, where the stress totally relaxes. When a free end of a dangling strand merges with a nearby junction at random time, the stress-free state of this strand coincides with the actual state of the network.

According to the other approach (the reptation theory [35]), relaxation of stresses in chains occurs due to (i) their curvilinear diffusion along the tubes formed by surrounding macromolecules, and (ii) partial release from the tubes, see Figures 6.1 and 6.4 in [35]. As a result of this motion, the reference state of a strand differs from that of the vector that connects its junction points. This idea provides a physical ground for the pom–pom model [31], where the average length of a strand in its stress-free state is introduced as an independent variable in the governing relations.

Despite evident merits of these concepts, they share an important shortcoming: these approaches lead to (i) a substantial complication of the constitutive equations and (ii) a noticeable increase in the number of material functions and parameters. To avoid an undesirable growth of experimental constants, on the one hand, and to make the constitutive equations thermodynamically consistent, on the other, we postulate that the characteristic rate of stress relaxation in strands (driven by their curvilinear diffusion in tubes or by their rearrangement in a transient network) substantially exceeds the rate of sliding of junctions. This implies that the number of strands per unit volume of a network N should be treated not as a constant, but as a function of time whose values are rapidly (compared to the characteristic time of the deformation process) tuned to those that are determined by the current state of the network (an estimate for the relaxation time will be provided in Section 9). Our hypothesis is in accord with the double reptation concept [36] that treat the response of a network of macromolecules as that induced by (i) rapid diffusive motion of chains in tubes (which is disregarded in the present model), and (ii) relatively slow relaxation of constrains imposed by surrounding macromolecules on the motion of a characteristic chain (which is accounted for in terms of the sliding process).

The assumption regarding two relaxation processes with different time scales implies that the Clausius–Duhem inequality (26) remains valid for relatively slow deformation processes with N thought of as a function of time (according to the Doi–Edwards theory [35], $N(t)$ is the number of strands per unit volume where stresses have not relaxed until instant t; in terms of the pom–pom model [31], $N(t)$ is proportional to the square of the stretch of a characteristic chain). According to this approach, the kinetic equation (30) remains unchanged, while the expression (28) for the stress tensor reads

$$\mathbf{\Sigma}(t) = -P(t)\mathbf{I} + 2N(t)\big(1 - \beta(t)\big)\Big[w_1(t)\mathbf{B}_{\mathrm{e}}(t) - w_2(t)\mathbf{B}_{\mathrm{e}}^{-1}(t)\Big], \tag{31}$$

where $N(t)$ is an adjustable function.

8

It is evident that the number of adjustable functions in Eqs. (30) and (31) is too large to find them with an acceptable level of accuracy by fitting experimental data in conventional rheological tests. To reduce this number, additional simplifications are conventionally introduced.

1. Assuming strands to be Gaussian with the strain energy density

$$w(J_{e1}, J_{e2}) = \frac{1}{2}\mu(J_{e1} - 3),\tag{32}$$

where μ is the average rigidity of a strand, setting $\alpha(t) = 0$ and $\gamma(t) = 0$, and using Eq. (18), we arrive at the relations

$$\boldsymbol{\Sigma}(t) = -P(t)\mathbf{I} + N(t)\mu\mathbf{B}_{e}(t),\tag{33}$$

$$\frac{d\mathbf{B}_{e}}{dt}(t) = \left(1 - \beta(t)\right)\left[\mathbf{D}(t) \cdot \mathbf{B}_{e}(t) + \mathbf{B}_{e}(t) \cdot \mathbf{D}(t)\right] + \left[\boldsymbol{\Omega}(t) \cdot \mathbf{B}_{e}(t) - \mathbf{B}_{e}(t) \cdot \boldsymbol{\Omega}(t)\right].\tag{34}$$

We now introduce the effective stress by the formula

$$\mathbf{T}(t) = N(t)\mu\mathbf{B}_{e}(t) - \Lambda(t)\mathbf{I},\tag{35}$$

where the function $\Lambda(t)$ will be specified later. Differentiation of Eq. (35) with respect to time t results in

$$\frac{d\mathbf{T}}{dt} = \frac{dN}{dt}(t)\mu\mathbf{B}_{e}(t) + N(t)\mu\frac{d\mathbf{B}_{e}}{dt}(t) - \frac{d\Lambda}{dt}(t)\mathbf{I}.$$

Substitution of Eqs. (34) and (35) into this equality implies that

$$\frac{d\mathbf{T}}{dt}(t) = \left(1 - \beta(t)\right)\left[\mathbf{D}(t) \cdot \mathbf{T}(t) + \mathbf{T}(t) \cdot \mathbf{D}(t)\right] + \left[\boldsymbol{\Omega}(t) \cdot \mathbf{T}(t) - \mathbf{T}(t) \cdot \boldsymbol{\Omega}(t)\right]$$

$$+ \frac{1}{N(t)}\frac{dN}{dt}(t)\mathbf{T}(t) + 2\left(1 - \beta(t)\right)\Lambda(t)\mathbf{D}(t) + \left[\frac{\Lambda(t)}{N(t)}\frac{dN}{dt}(t) - \frac{d\Lambda}{dt}(t)\right]\mathbf{I}.\tag{36}$$

The function $\Lambda(t)$ is determined from the condition that the last term on the right-hand side of Eq. (36) vanishes,

$$\Lambda(t) = CN(t),$$

where C is an arbitrary constant. Setting

$$\frac{1}{N(t)}\frac{dN}{dt}(t) = -\frac{1}{\tau(t)},$$

where $\tau(t)$ is a new material function (the characteristic time for rearrangement of tubes according to the reptation theory), we find that

$$N(t) = N(0)\exp\left[-\int_{0}^{t}\tau(s)ds\right].$$

Substitution of these expressions into Eq. (36) results in the constitutive equation of the Johnson–Segalman model [32],

$$\frac{d\mathbf{T}}{dt}(t) = \left(1 - \beta(t)\right)\left[\mathbf{D}(t) \cdot \mathbf{T}(t) + \mathbf{T}(t) \cdot \mathbf{D}(t)\right] + \left[\boldsymbol{\Omega}(t) \cdot \mathbf{T}(t) - \mathbf{T}(t) \cdot \boldsymbol{\Omega}(t)\right]$$

$$+ \frac{1}{\tau(t)}\left[2\eta(t)\mathbf{D}(t) - \mathbf{T}(t)\right],\tag{37}$$

9

where the viscosity η is given by

$$\eta(t) = CN_0\big(1 - \beta(t)\big)\tau(t)\exp\Big[-\int_0^t \tau(s)ds\Big].$$

2. Adopting hypothesis (32) and setting $\alpha(t) = 0$ and $\gamma(t) = 0$, we find that

$$\begin{aligned}
\mathbf{\Sigma}(t) &= -P(t)\mathbf{I} + N(t)\mu\big(1 - \beta(t)\big)\mathbf{B}_{\mathrm{e}}(t), \\
\mathbf{B}_{\mathrm{e}}^{\triangle}(t) &= -\beta(t)\big[\mathbf{D}(t)\cdot\mathbf{B}_{\mathrm{e}}(t) + \mathbf{B}_{\mathrm{e}}(t)\cdot\mathbf{D}(t)\big],
\end{aligned}$$

where

$$\mathbf{B}_{\mathrm{e}}^{\triangle}(t) = \frac{d\mathbf{B}_{\mathrm{e}}}{dt}(t) - \mathbf{L}(t)\cdot\mathbf{B}_{\mathrm{e}}(t) - \mathbf{B}_{\mathrm{e}}(t)\cdot\mathbf{L}^{\top}(t)$$

is the Oldroyd contravariant derivative. Introducing the effective stress $\mathbf{T}(t)$ by Eq. (35), we obtain

$$\begin{aligned}
\mathbf{T}^{\triangle}(t) &= -\beta(t)\big[\mathbf{D}(t)\cdot\mathbf{T}(t) + \mathbf{T}(t)\cdot\mathbf{D}(t)\big] + \frac{1}{N(t)}\frac{dN}{dt}(t)\mathbf{T}(t) \\
&\quad + 2\big(1 - \beta(t)\big)\Lambda(t)\mathbf{D}(t) + \Big[\frac{\Lambda(t)}{N(t)}\frac{dN}{dt}(t) - \frac{d\Lambda}{dt}(t)\Big]\mathbf{I}.
\end{aligned}$$

Equating the last term in the right-hand side of this formula to zero, we arrive at the Phan-Thien–Tanner constitutive model [33]

$$\mathbf{T}^{\triangle}(t) = -\beta(t)\big[\mathbf{D}(t)\cdot\mathbf{T}(t) + \mathbf{T}(t)\cdot\mathbf{D}(t)\big] + \frac{1}{\tau(t)}\big[2\eta(t)\mathbf{D}(t) - \mathbf{T}(t)\big]. \qquad (38)$$

3. Accepting formula Eq. (32) for the strain energy of a Gaussian strand and assuming that $\beta(t) = 0$ and $\gamma(t) = 0$, we find that the Cauchy stress tensor $\mathbf{\Sigma}(t)$ is given by Eq. (33), where the function $\mathbf{B}_{\mathrm{e}}(t)$ is governed by the differential equation

$$\mathbf{B}_{\mathrm{e}}^{\triangle}(t) = -\alpha(t)\mu\Big[\mathbf{B}_{\mathrm{e}}^2(t) - \frac{1}{3}J_{\mathrm{e}1}(t)\mathbf{B}_{\mathrm{e}}(t)\Big].$$

Substitution of expression (35) for the effective stress $\mathbf{T}(t)$ into this equality implies that

$$\begin{aligned}
\mathbf{T}^{\triangle}(t) &= \Big[\frac{1}{N(t)}\frac{dN}{dt}(t) + 2\frac{\alpha(t)\Lambda(t)}{N(t)} - \frac{1}{3}\alpha\mu J_{\mathrm{e}1}(t)\Big]\mathbf{T}(t) - \frac{\alpha(t)}{N(t)}\mathbf{T}^2(t) \\
&\quad + 2\Lambda(t)\mathbf{D}(t) + \Big[\frac{\Lambda(t)}{N(t)}\frac{dN}{dt}(t) - \frac{\alpha(t)}{N(t)}\Lambda^2(t) - \frac{1}{3}\alpha(t)\mu\Lambda(t)J_{\mathrm{e}1}(t) - \frac{d\Lambda}{dt}(t)\Big]\mathbf{I}.
\end{aligned}$$

Equating the last term of the right-hand side of this equation to zero, which results in the differential equation for the function $\Lambda(t)$,

$$\frac{d\Lambda}{dt}(t) = \Lambda(t)\Big[\frac{1}{N(t)}\frac{dN}{dt}(t) - \frac{\alpha(t)}{N(t)}\Lambda(t) - \frac{1}{3}\alpha(t)\mu J_{\mathrm{e}1}(t)\Big],$$

and introducing the new adjustable functions

$$\tau(t) = -\Big[\frac{1}{N(t)}\frac{dN}{dt}(t) + 2\frac{\alpha(t)\Lambda(t)}{N(t)} - \frac{1}{3}\alpha\mu J_{\mathrm{e}1}(t)\Big], \qquad \eta(t) = \Lambda(t)\tau(t),$$

10

we arrive at the formula

$$\mathbf{T}^\triangle(t) + \frac{\alpha(t)}{N(t)}\mathbf{T}^2(t) = \frac{1}{\tau(t)}\Big[2\eta(t)\mathbf{D}(t) - \mathbf{T}(t)\Big], \tag{39}$$

which coincides with the Giesekus constitutive equation [24].

It is worth noting that the material functions $\tau(t)$ and $\eta(t)$ in Eqs. (37) to (39) are not arbitrary, but they obey some additional restrictions. This is caused by the fact that we consider relaxation of stresses in strands driven by their diffusion inside tubes as a rapid process compared to rearrangement of tubes (treated as sliding of junctions). An advantage of our approach is that it operates with the Cauchy deformation tensors conventionally employed in continuum mechanics (no configurational tensors are introduced) and is based on the classical multiplicative decomposition of the deformation gradient (unlike constitutive equations that explicitly use a slip tensor).

4. Finally, under the assumptions that (i) w is a symmetric function of its arguments, which implies that

$$w_1(t) = w_2(t) = \bar{w}(t),$$

and (ii) the functions $\beta(t)$ and $\gamma(t)$ vanish, Eqs. (28) and (31) are transformed into the Leonov constitutive model [34]

$$
\begin{aligned}
\boldsymbol{\Sigma}(t) &= -P(t)\mathbf{I} + 2N(t)\bar{w}(t)\Big(\mathbf{B}_{\mathrm{e}}(t) - \mathbf{B}_{\mathrm{e}}^{-1}(t)\Big), \\
\mathbf{B}_{\mathrm{e}}^\triangle(t) &= -2\alpha(t)\bar{w}(t)\Big[\mathbf{B}_{\mathrm{e}}^2(t) + \frac{1}{3}\Big(J_{\mathrm{e}2}(t) - J_{\mathrm{e}1}(t)\Big)\mathbf{B}_{\mathrm{e}}(t) - \mathbf{I}\Big].
\end{aligned}
$$

Unlike the above approaches, this study focuses on the case when the functions $\beta(t)$ and $\gamma(t)$ coincide,

$$\gamma(t) = \beta(t) = b(t). \tag{40}$$

This allows us to omit the second term on the right-hand side of Eq. (30), which may result in stress oscillations at simple shear that have no physical meaning. From the kinematic standpoint, condition (40) means that the velocity gradients for sliding of junctions and macro-deformation are connected by the linear equation, see Eqs. (18) and (23),

$$\mathbf{L}_{\mathrm{s}}(t) = b(t)\mathbf{L}(t) + \mathbf{M}(t),$$

where $\mathbf{M}(t)$ is a symmetric traceless tensor given by Eq. (29). Substitution of expression (40) into Eq. (30) implies the differential equation

$$
\begin{aligned}
\frac{d\mathbf{B}_{\mathrm{e}}}{dt}(t) &= \Big(1 - b(t)\Big)\Big[\mathbf{L}(t) \cdot \mathbf{B}_{\mathrm{e}}(t) + \mathbf{B}_{\mathrm{e}}(t) \cdot \mathbf{L}^\top(t)\Big] \\
&\quad -2\alpha(t)\Big[w_1(t)\mathbf{B}_{\mathrm{e}}^2(t) + \frac{1}{3}\Big(w_2(t)J_{\mathrm{e}2}(t) - w_1(t)J_{\mathrm{e}1}(t)\Big)\mathbf{B}_{\mathrm{e}}(t) - w_2(t)\mathbf{I}\Big]. \tag{41}
\end{aligned}
$$

For a network of Gaussian strands, see Eq. (32), the stress–strain relations (31) and (41) read

$$
\begin{aligned}
\boldsymbol{\Sigma}(t) &= -P(t)\mathbf{I} + G(t)\Big(1 - b(t)\Big)\mathbf{B}_{\mathrm{e}}(t), \\
\frac{d\mathbf{B}_{\mathrm{e}}}{dt}(t) &= \Big(1 - b(t)\Big)\Big[\mathbf{L}(t) \cdot \mathbf{B}_{\mathrm{e}}(t) + \mathbf{B}_{\mathrm{e}}(t) \cdot \mathbf{L}^\top(t)\Big] - a(t)\Big[\mathbf{B}_{\mathrm{e}}^2(t) - \frac{1}{3}J_{\mathrm{e}1}(t)\mathbf{B}_{\mathrm{e}}(t)\Big] \tag{42}
\end{aligned}
$$

11

with

$$a(t) = \alpha(t)\mu, \qquad G(t) = \mu N(t).$$

Our aim now is to specify the dependencies of a, b and G in Eqs. (42) on parameters that characterize macro-deformation of a polymer fluid.

4 Adjustable functions

We introduce the rate intensity D_i by the conventional formula $D_i = \left(2\mathbf{D} : \mathbf{D}\right)^{\frac{1}{2}}$ and adopt the following equation for the elastic modulus G:

$$\frac{\ln G}{\ln G_0} = \exp\left(K_G D_i^{\nu_G}\right), \tag{43}$$

where G_0, K_G and ν_G are non-negative material constants. According to Eq. (43), G_0 is the plateau modulus at small strain rates, whereas K_G and ν_G characterize a strong increase in G with strain-rate intensity.

The parameter b is assumed to obey the power law,

$$b = K_b D_i^{\nu_b} \tag{44}$$

with non-negative adjustable parameters K_b and ν_b. Formula (44) means that no sliding of junctions occurs at very small strain rates, and the rate of sliding grows with the rate of macro-strain. Equations (43) and (44) are applicable within a limited range of strain rates, as the modulus G and the parameter b should reach some limiting values at sufficiently high strain rates.

The coefficient a is split into the product of two functions

$$a = \zeta A, \tag{45}$$

where the function ζ characterizes the effect of strain and the function A determines the effect of strain rate on the rate of energy dissipation [described by means of the coefficient a that is proportional to α in Eqs. (26) and (29)].

The dependence of the parameter A on strain-rate intensity D_i is determined by the power-law similar to Eq. (44),

$$A = A_0 + K_A D_i^{\nu_A}, \tag{46}$$

where A_0, K_A and ν_A are non-negative coefficients. Eq. (46) means that A monotonically increases with strain rate from its plateau value A_0. Unlike Eq. (44) for the function $b(D_i)$, we do not presume A to vanish at small strain rates; a reason for this claim will be explained later in Section 9.

It seems natural to suppose that for a developed flow with large strains, the motion of junctions at the micro-level is affine with macro-deformation. It follows from Eqs. (23) and (40) that this hypothesis is tantamount to the assertion that the coefficient α in Eq. (29) vanishes. This conclusion implies that ζ should approach zero at large deformations (that is at large strain energies). To approximate such a dependence, the exponential function is chosen,

$$\zeta = \exp\left[-r(J_{e1} - 3)\right], \tag{47}$$

12

where $r \geq 0$ is a constant. Our choice of the term $J_{e1} - 3$ in Eq. (47) may be justified by the fact that this expression is proportional to the strain energy of a Gaussian strand (32). Combining Eqs. (45) to (47), we arrive at the formula

$$a = \left(A_0 + K_A D_i^{\nu_A} \right) \exp \left[-r(J_{e1} - 3) \right].$$ (48)

Formally, Eqs. (42) to (44) and (48) involve 9 adjustable parameters: A_0, G_0, K_A, K_b, K_G, ν_A, ν_b, ν_G and r. It should be noted, however, that any set of experimental data at an arbitrary deformation with a constant strain-rate intensity D_i is determined by 4 constants only: A, b, G and r. The other quantities can be found by fitting the functions $A(D_i)$, $b(D_i)$ and $G(D_i)$ by Eqs. (43), (44) and (46).

Our aim now is to apply constitutive equations (42) for the analysis of uniaxial extension and simple shear of a polymer fluid.

5   Uniaxial extension

Uniaxial extension of an incompressible medium is described by the formulas

$$x_1 = k(t)X_1, \qquad x_2 = k^{-\frac{1}{2}}(t)X_2, \qquad x_3 = k^{-\frac{1}{2}}(t)X_3,$$ (49)

where $\{X_i\}$ are Cartesian coordinates in the initial state, $\{x_i\}$ are Cartesian coordinates in the deformed state, and $k = k(t)$ stands for elongation. We suppose that transition from the initial state to the current reference state that determines the sliding process is described by the equations similar to Eqs. (49),

$$\xi_1 = \kappa(t)X_1, \qquad \xi_2 = \kappa^{-\frac{1}{2}}(t)X_2, \qquad \xi_3 = \kappa^{-\frac{1}{2}}(t)X_3,$$ (50)

where $\{\xi_i\}$ are Cartesian coordinates in the intermediate state, and $\kappa = \kappa(t)$ is a function to be found. According to Eqs. (49) and (50), the deformation gradients $\mathbf{F}$ and $\mathbf{F}_s$ are given by

$$\mathbf{F} = k\mathbf{e}_1\mathbf{e}_1 + k^{-\frac{1}{2}}(\mathbf{e}_2\mathbf{e}_2 + \mathbf{e}_3\mathbf{e}_3), \qquad \mathbf{F}_s = \kappa\mathbf{e}_1\mathbf{e}_1 + \kappa^{-\frac{1}{2}}(\mathbf{e}_2\mathbf{e}_2 + \mathbf{e}_3\mathbf{e}_3),$$ (51)

where $\mathbf{e}_i$ are unit vectors of the frame $\{X_i\}$. It follows from Eqs. (1), (8) and (51) that

$$\mathbf{B}_e = \left(\frac{k}{\kappa} \right)^2 \mathbf{e}_1\mathbf{e}_1 + \frac{\kappa}{k}(\mathbf{e}_2\mathbf{e}_2 + \mathbf{e}_3\mathbf{e}_3)$$

and

$$J_{e1} = \left(\frac{k}{\kappa} \right)^2 + 2\frac{\kappa}{k}.$$

The velocity gradient $\mathbf{L}$, the rate-of-strain tensor $\mathbf{D}$, and the strain-rate intensity D_i read

$$\mathbf{L} = \mathbf{D} = \frac{\dot{k}}{k}\left[\mathbf{e}_1\mathbf{e}_1 - \frac{1}{2}(\mathbf{e}_2\mathbf{e}_2 + \mathbf{e}_3\mathbf{e}_3) \right], \qquad D_i = \frac{|\dot{k}|}{k}\sqrt{3},$$ (52)

where $\dot{k} = dk/dt$. Substitution of these expressions into Eqs. (42) results in the differential equation for the function $\kappa(t)$,

$$\frac{\dot{\kappa}}{\kappa} = b\frac{\dot{k}}{k} + \frac{a}{3}\left[\left(\frac{k}{\kappa} \right)^2 - \frac{\kappa}{k} \right], \qquad \kappa(0) = 1.$$ (53)

13

The Cauchy stress tensor $\mathbf{\Sigma}$ is given by

$$\mathbf{\Sigma} = \Sigma_1 \mathbf{e}_1 \mathbf{e}_1 + \Sigma_2 (\mathbf{e}_2 \mathbf{e}_2 + \mathbf{e}_3 \mathbf{e}_3),$$

where the stress difference $\Delta\Sigma = \Sigma_1 - \Sigma_2$ reads

$$\Delta\Sigma = G(1-b)\Big[\Big(\frac{k}{\kappa}\Big)^2 - \frac{\kappa}{k}\Big]. \tag{54}$$

Given a deformation program $k(t)$, Eqs. (53) and (54) together with the phenomenological equations (43), (44) and (48) determine the stress difference $\Delta\Sigma$ as a function of time.

For uniaxial extension with a constant rate of Hencky strain

$$\frac{\dot{k}}{k} = \dot{\epsilon},$$

it is natural to search a solution of Eq. (53) in the form

$$\kappa(t) = z(t)\exp(\dot{\epsilon}t), \tag{55}$$

where $z(t)$ is a function to be found. Substituting expression (55) into Eq. (53) and using Eq. (48), we find that

$$\dot{z} + (1-b)\dot{\epsilon}z = \frac{A}{3z}(1-z^3)\exp\Big(-r\frac{1-3z^2+2z^3}{z^2}\Big), \qquad z(0) = 1, \tag{56}$$

where A, b and G depends on $\dot{\epsilon}$. It follows from Eq. (56) that when $t \to \infty$, the function $z(t)$ approaches its limiting value z_0, which is determined by the nonlinear equation

$$\frac{1-z_0^3}{z_0^2}\exp\Big(-r\frac{1-3z_0^2+2z_0^3}{z_0^2}\Big) = \frac{3(1-b)\dot{\epsilon}}{A}. \tag{57}$$

According to Eqs. (54) and (55), the transient elongational viscosity

$$\eta_e^+ = \frac{\Delta\Sigma}{\dot{\epsilon}} \tag{58}$$

is given by

$$\eta_e^+ = G(1-b)\frac{1-z^3}{\dot{\epsilon}z^2}.$$

Equation Eq. (57) implies that when $t \to \infty$, the transient viscosity η_e^+ tends to its limiting value

$$\eta_e = \frac{3G}{A}(1-b)^2\exp\Big(r\frac{1-3z_0^2+2z_0^3}{z_0^2}\Big).$$

This formula together with Eq. (57) determine the steady elongational viscosity η_e as a function of the Hencky strain rate $\dot{\epsilon}$. When $r = 0$ (no effect of strain on the coefficient a), we find that

$$\eta_e = \frac{3G}{A}(1-b)^2. \tag{59}$$

According to Eqs. (44) and (48), Eq. (59) describes a pronounced decrease in the steady elongational viscosity at large strain rates observed in numerous experiments.

6 Simple shear

Simple shear of an incompressible medium is described by the equations

$$x_1 = X_1 + k(t)X_2, \qquad x_2 = X_2, \qquad x_3 = X_3, \tag{60}$$

where $\{X_i\}$ and $\{x_i\}$ are Cartesian coordinates in the initial and actual states, respectively, and $k(t)$ stands for shear. We describe transition from the initial to the intermediate configuration that characterizes sliding of junctions as a superposition of simple shear and three-dimensional extension,

$$\xi_1 = \lambda_1(t)X_1 + \kappa(t)X_2, \qquad \xi_2 = \lambda_2(t)X_2, \qquad \xi_3 = \lambda_3(t)X_3, \tag{61}$$

where $\{\xi_i\}$ are Cartesian coordinates in the stress-free state, and $\lambda_i(t)$ and $\kappa(t)$ are functions to be found. The functions $\lambda_i(t)$ obey the incompressibility condition

$$\lambda_1 \lambda_2 \lambda_3 = 1.$$

It follows from Eqs. (60) and (61) that the deformation gradients $\mathbf{F}$ and $\mathbf{F}_s$ read

$$
\begin{aligned}
\mathbf{F} &= \mathbf{e}_1\mathbf{e}_1 + \mathbf{e}_2\mathbf{e}_2 + \mathbf{e}_3\mathbf{e}_3 + k\mathbf{e}_1\mathbf{e}_2, \\
\mathbf{F}_s &= \lambda_1\mathbf{e}_1\mathbf{e}_1 + \lambda_2\mathbf{e}_2\mathbf{e}_2 + \lambda_3\mathbf{e}_3\mathbf{e}_3 + \kappa\mathbf{e}_1\mathbf{e}_2.
\end{aligned}
$$

Substitution of these expressions into Eq. (1) implies that

$$\mathbf{F}_e = p_1\mathbf{e}_1\mathbf{e}_1 + p_2\mathbf{e}_2\mathbf{e}_2 + p_3\mathbf{e}_3\mathbf{e}_3 + \phi\mathbf{e}_1\mathbf{e}_2, \tag{62}$$

where

$$p_1 = \lambda_2\lambda_3, \qquad p_2 = \lambda_1\lambda_3, \qquad p_3 = \lambda_1\lambda_2, \qquad \phi = \lambda_3(\lambda_1 k - \kappa).$$

In the new notation, the incompressibility condition is given by

$$p_1 p_2 p_3 = 1. \tag{63}$$

It follows from Eqs. (8) and (62) that the left Cauchy–Green tensor for elastic deformation is determined as

$$\mathbf{B}_e = (p_1^2 + \phi^2)\mathbf{e}_1\mathbf{e}_1 + p_2^2\mathbf{e}_2\mathbf{e}_2 + p_3^2\mathbf{e}_3\mathbf{e}_3 + p_2\phi(\mathbf{e}_1\mathbf{e}_2 + \mathbf{e}_2\mathbf{e}_1). \tag{64}$$

The velocity gradient $\mathbf{L}$, the rate-of-strain tensor $\mathbf{D}$, and the strain-rate intensity D_i read

$$\mathbf{L} = \dot{k}\mathbf{e}_1\mathbf{e}_2, \qquad \mathbf{D} = \frac{1}{2}\dot{k}(\mathbf{e}_1\mathbf{e}_2 + \mathbf{e}_2\mathbf{e}_1), \qquad D_i = \dot{k}. \tag{65}$$

We substitute expressions (64) and (65) into the second equation in Eqs. (42). Omitting simple but tedious algebra, we arrive at the following equations:

$$
\begin{aligned}
\dot{p}_1 &= -\frac{a}{6}p_1(2p_1^2 - p_2^2 - p_3^2 - \phi^2), & p_1(0) &= 1, \\
\dot{p}_2 &= -\frac{a}{6}p_2(-p_1^2 + 2p_2^2 - p_3^2 + 2\phi^2), & p_2(0) &= 1, \\
\dot{p}_3 &= -\frac{a}{6}p_1(-p_1^2 - p_2^2 + 2p_3^2 - \phi^2), & p_3(0) &= 1, \\
\dot{\phi} &= (1-b)\dot{k}p_2 - \frac{a}{6}\phi(5p_1^2 + 2p_2^2 - p_3^2 + 2\phi^2), & \phi(0) &= 0.
\end{aligned}
\tag{66}
$$

It is easy to check that Eqs. (66) imply the incompressibility condition (63) for an arbitrary deformation program $k(t)$. Combining Eqs. (42) and (64), we obtain

$$\boldsymbol{\Sigma} = \Sigma_{11}\mathbf{e}_1\mathbf{e}_1 + \Sigma_{22}\mathbf{e}_2\mathbf{e}_2 + \Sigma_{33}\mathbf{e}_3\mathbf{e}_3 + \Sigma_{12}\phi(\mathbf{e}_1\mathbf{e}_2 + \mathbf{e}_2\mathbf{e}_1),$$

where

$$
\begin{aligned}
\Sigma_{11} &= -P + G(1-b)(p_1^2 + \phi^2), \\
\Sigma_{22} &= -P + G(1-b)p_2^2, \\
\Sigma_{33} &= -P + G(1-b)p_3^2, \\
\Sigma_{12} &= G(1-b)p_2\phi.
\end{aligned}
\tag{67}
$$

It follows from these equations that the first normal stress difference $N_1^+ = \Sigma_{11} - \Sigma_{22}$ and the second normal stress difference $N_2^+ = \Sigma_{22} - \Sigma_{33}$ read

$$N_1^+ = G(1-b)(p_1^2 - p_2^2 + \phi^2), \qquad N_2^+ = G(1-b)(p_2^2 - p_3^2). \tag{68}$$

Equations (66) to (68) describe the time-dependent response of a polymer fluid under shear with an arbitrary deformation program $k(t)$. Our aim now is to analyze these equations for shearing with a constant strain rate $\dot{k}$ and to study their steady-state solutions at $t \to \infty$. Assuming that $p_i(t) \to p_{i0}$ and $\phi(t) \to \phi_0$ as $t \to \infty$, we find from Eqs. (66) that the limiting values p_{i0} and ϕ_0 satisfy the algebraic equations

$$
\begin{aligned}
2p_{10}^2 - p_{20}^2 - p_{30}^2 - \phi_0^2 &= 0, \\
-p_{10}^2 + 2p_{20}^2 - p_{30}^2 + 2\phi_0^2 &= 0, \\
-p_{10}^2 - p_{20}^2 + 2p_{30}^2 - \phi_0^2 &= 0.
\end{aligned}
\tag{69}
$$

To derive these equations, the incompressibility condition (63) is employed which excludes the case when any of p_{i0} vanishes. Subtracting the third equality in Eqs. (69) from the first, we find that

$$p_{30}^2 = p_{10}^2. \tag{70}$$

Substitution of expression (70) into the first equality in Eqs. (69) results in

$$p_{10}^2 = p_{20}^2 + \phi_0^2. \tag{71}$$

Combining Eqs. (63), (70) and (71), we obtain

$$p_{20}(p_{20}^2 + \phi_0^2) = 1. \tag{72}$$

It follows from Eqs. (66) that ϕ_0 satisfies the equation

$$(1-b)\dot{k}p_{20} = \frac{1}{6}\zeta_0 A\phi_0(5p_{10}^2 + 2p_{20}^2 - p_{30}^2 + 2\phi_0^2),$$

where, according to Eqs. (46) and (64),

$$\zeta_0 = \exp\left[-r\left(p_{10}^2 + p_{20}^2 + p_{30}^2 + \phi_0^2 - 3\right)\right].$$

16

Substitution of expressions (70) and (71) into these equations implies that

$$\phi_0(p_{20}^2 + \phi_0^2) = \frac{(1-b)\dot{k}}{\zeta_0 A}p_{20}, \qquad \zeta_0 = \exp\left[-3r\left(p_{20}^2 + \phi_0^2 - 1\right)\right].$$

Excluding the sum $p_{20}^2 + \phi_0^2$ by means of Eq. (72), we find that

$$\phi_0 = \frac{(1-b)\dot{k}}{A}p_{20}^2 \exp\left[3r(p_{20}^{-1} - 1)\right]. \tag{73}$$

Finally, substitution of expression (73) into Eq. (72) results in the transcendental equation for p_{20},

$$p_{20}^3\left[1 + \frac{(1-b)^2\dot{k}^2}{A^2}p_{20}^2 \exp\left(6r(p_{20}^{-1} - 1)\right)\right] = 1. \tag{74}$$

It follows from Eqs. (67) that the shear stress Σ_{12} tends to its limiting value

$$\Sigma_{12\,0} = G(1-b)p_{20}\phi_0$$

when t approaches infinity. Substituting expression (73) into this formula and introducing the steady shear viscosity

$$\eta_s = \frac{\Sigma_{12\,0}}{\dot{k}},$$

we obtain

$$\eta_s = \frac{G}{A}(1-b)^2 p_{20}^3 \exp\left[3r(p_{20}^{-1} - 1)\right]. \tag{75}$$

In the case when $r = 0$, which is equivalent to the neglect of the influence of strain on the coefficient a, Eq. (75) reads

$$\eta_s = \frac{G}{A}(1-b)^2 p_{20}^3. \tag{76}$$

Comparing Eqs. (59) and (76) and introducing the Trouton ratio

$$\mathrm{Tr} = \frac{\eta_e}{\eta_s},$$

we obtain

$$\mathrm{Tr} = 3p_{20}^{-3}.$$

Combining this formula with Eq. (74) (where we set $r = 0$) and bearing in mind Eq. (65), we arrive at the equation for the Trouton ratio

$$\mathrm{Tr} = 3\left\{1 + \left[\frac{3^{\frac{1}{3}}(1-b)D_i}{A}\right]^2 \mathrm{Tr}^{-\frac{2}{3}}\right\}.$$

This formula implies that under the condition $\nu_G < 1$, the Trouton ratio equals 3 at very small strain rates, and it increases with the strain-rate intensity, at least at relatively small D_i, in agreement with the experimental data reported in [37].

We return now to the general case $r \geq 0$ and calculate the limiting values N_1 and N_2 of the normal stress differences when $t \to \infty$. It follows from Eqs. (68), (70) and (71) that

$$N_1 = 2G(1-b)\phi_0^2, \qquad N_2 = -G(1-b)\phi_0^2.$$

17

Introducing the steady normal stress functions $\Psi_i = N_i \dot{k}^{-2}$ and using Eq. (73), we find that

$$\Psi_1 = \frac{2G}{A^2}(1-b)^3 p_{20}^4 \exp\left[6r(p_{20}^{-1} - 1)\right], \qquad \Psi_2 = -\frac{1}{2}\Psi_1. \tag{77}$$

Equations (74), (75) and (77) together with the phenomenological relations (43), (44) and (46) determine the steady shear viscosity and normal stress functions for an arbitrary shear rate $\dot{k}$. Equation (77) correctly predicts that the second normal stress coefficient Ψ_2 is negative and proportional to the first normal stress function Ψ_1. It is conventionally assumed for polymer fluids that the coefficient of proportionality between Ψ_1 and Ψ_2 should be of order of 0.1 to 0.3 [37], but the ratio $|\Psi_2|/\Psi_1$ is strongly affected by experimental conditions, and its precise value remains unknown [38]. Recent experiments on suspension in viscous fluids show that this ratio is located in the interval between 0.1 and 0.7 with the most probable value of 0.5 for highly viscous liquids [39]. The latter result is in excellent agreement with Eqs. (77).

7   Fitting of observations

Our aim now is to demonstrate that constitutive equations (42) can correctly approximate observations in start-up shear tests with various strain rates and to show that the adjustable parameters change consistently with shear rate and characteristics of molecular weight distribution. For this purpose, we focus on three sets of experimental data for solutions of polystyrene in tricresyl phosphate. For a detailed description of the experimental procedure and the material properties, we refer to the original studies [11, 12, 13]. The main parameters of the solutions (abbreviated here as PS1, PS2 and PS3) are collected in Table 1. The polydispersity index of PS2 and PS3 are not provided, but it is mentioned that they have "sharp molecular weight distributions" [12, 13]. Based on these observations, we treat the solutions as monodisperse and concentrate on the effects of mass-average molecular weight M_w and the number of entanglements per chain M_w/M_e (M_e stands for the average molecular weight between entanglements) on material constants.

We begin with fitting the observations on PS1 for the shear stress Σ_{12} and the first normal stress difference N_1^+ depicted in Figures 1 and 2. These figures show that the functions $\Sigma_{12}(t)$ and $N_1^+(t)$ increase monotonically with time at small shear rates $\dot{k}$ and demonstrate pronounced stress overshoots at relatively large $\dot{k}$. As the experimental data were reported in Figure 4 of [11] with the use of the regular time-scale, we follows the same approach. The other sets of data (see Figures 6 to 8 below) are presented in the logarithmic time-scale ($\log = \log_{10}$) that makes more transparent the characteristic features of stress overshoot.

First, we approximate the experimental dependencies $\Sigma_{12}(t)$ and $N_1^+(t)$ measured at the highest strain rate $\dot{k}_{max} = 4.0\ \mathrm{s}^{-1}$, by using four constants, A, b, G and r [the coefficient a in Eqs. (66) is calculated from Eq. (45), where ζ is given by Eq. (47)]. To find the coefficients A, b, G and r, we fix some intervals $[0, A_{max}]$, $[0, b_{max}]$, $[0, G_{max}]$ and $[0, r_{max}]$, where the "best-fit" parameters A, b, G and r are assumed to be located, and divide these intervals into J subintervals by the points $A^{(i)} = i\Delta A$, $b^{(j)} = j\Delta b$, $G^{(k)} = k\Delta G$ and $r^{(l)} = l\Delta r$ ($i, j, k, l = 1, \ldots, J-1$) with $\Delta A = A_{max}/J$, $\Delta b = b_{max}/J$, $\Delta G = G_{max}/J$ and $\Delta r = r_{max}/J$. For any set $\{A^{(i)}, b^{(j)}, G^{(k)}, r^{(l)}\}$, Eqs. (66) are integrated numerically by the Runge–Kutta

18

method with the time-step $\Delta t = 1.0 \cdot 10^{-3}$ s^{-1}, and the quantities Σ_{12} and N_1^+ are calculated from Eqs. (67) and (68). The "best-fit" parameters A, b, G and r are determined from the condition of minimum of the function

$$R = \sum_{t_m} \left\{ \left[\Sigma_{12}^{\text{exp}}(t_m) - \Sigma_{12}^{\text{num}}(t_m) \right]^2 + \delta \left[N_1^{\text{exp}}(t_m) - N_1^{\text{num}}(t_m) \right]^2 \right\} \tag{78}$$

on the set $\{A^{(i)}, b^{(j)}, G^{(k)}, r^{(l)} \ (i, j, k, l = 1, \ldots, J-1)\}$. Here the coefficient δ characterizes a "weight" of the second term compared to the first one, the sum is calculated over all experimental points t_m depicted in Figures 1 and 2, Σ_{12}^{exp} and N_1^{exp} are the shear stress and the first normal stress difference measured in a test, and Σ_{12}^{num} and N_1^{num} are given by Eqs. (67) and (68). In the numerical analysis, we set $J = 10$ and $\delta = 0.05$. After finding the "best-fit" values $A^{(i)}$, $b^{(j)}$, $G^{(k)}$ and $r^{(l)}$, this procedure is repeated twice for the new intervals $[A^{(i-1)}, A^{(i+1)}]$, $[b^{(j-1)}, b^{(j+1)}]$, $[G^{(k-1)}, G^{(k+1)}]$ and $[r^{l-1}, r^{(l+1)}]$, to ensure an acceptable accuracy of fitting.

After finding the "best-fit" value of r by matching the data obtained at $\dot{k}_{\text{max}}$, we fix this parameter and approximate the observations at other shear rates with the help of only three material constants, A, b and G. Each pair of curves (for Σ_{12} and N_1^+) measured at a given shear rate $\dot{k}$ is matched separately.

Figures 1 and 2 demonstrate good agreement between the experimental data and the results of numerical simulation. The model correctly predicts that the shear stress Σ_{12} reaches its maximum before the first normal stress difference N_1^+ approaches its highest value. It is worth mentioning that the quality of fitting observations in Figures 1 and 2 is substantially better than that reported for other constitutive models in [29] (underprediction of the shear stress) and in [27] (overprediction of Σ_{12}).

The quantities A, b and G are plotted in Figures 3 to 5 versus shear rate $\dot{k}$. The function $A(\dot{k})$ in Figure 3 is approximated by the simplified version of Eq. (46) with $A_0 = 0$. Bearing in mind expression (65) for D_i, we present Eqs. (44) and (46) in the form

$$\log A = \log K_A + \nu_A \log \dot{k}, \qquad \log b = \log K_b + \nu_b \log \dot{k}. \tag{79}$$

The coefficients K_A, K_b, ν_A and ν_b in Eqs. (79) are determined by the least-squares technique. The function $G(\dot{k})$ in Figure 5 is fitted by Eq. (43), where the coefficients G_0, K_G and ν_G are found by the nonlinear regression algorithm. These quantities are listed in Table 2. Figures 3 to 5 show reasonable agreement between the experimental data and their approximations by Eqs. (43) and (79).

We proceed with fitting observations for polystyrene solutions PS2 and PS3, where we confine ourselves to matching experimental data for the shear stress Σ_{12} only. The same algorithm of fitting is employed as for PS1, with the only exception that the last term in Eq. (78) is omitted ($\delta = 0$).

The experimental dependencies $\Sigma_{12}(t)$ measured at various strain rates $\dot{k}$ are plotted together with the results of numerical simulation in Figure 6 for PS2 and in Figure 7 for PS3. These figures demonstrate good agreement between the observations and the results of numerical analysis at all strain rates under consideration. It is worth noting that the model can correctly reproduce not only stress overshoot, but also weak stress undershoot revealed in experiments. The adjustable parameters A, b and G are presented in Figures 3

to 5 as functions of shear rate together with their approximations by Eqs. (43) and (79). The "best-fit" values of the parameter r are collected in Table 2.

Our aim now is to discuss the effects of strain rate and molecular weight of polystyrene solutions on the adjustable parameters in the constitutive equations.

8   Discussion

According to Figure 5, the elastic modulus G grows with strain-rate intensity D_i for all solutions. It follows from Table 2 that the rate of increase in G [the exponent ν_G in Eq. (43)] monotonically decreases with number of entanglements per chain $M_\mathrm{w}/M_\mathrm{e}$. This observation appears to be natural if we treat changes in G with strain rate within the Doi–Edwards reptation theory as a result of rearrangement of tubes driven by macro-deformation. The latter implies that changes in the number of non-relaxed strands with $\dot{k}$ should be extremely pronounced for a weakly entangled network (where a strand is practically the same as a chain), and should be relatively weak for a strongly entangled system (where the number of entanglements per chain is rather large, and only strands located at the ends of a chain can easily escape from the tubes).

The other parameter that characterizes the effect of strain rate on the elastic modulus, the coefficient K_G in Eq. (43), appears to correlate with mass-average molecular weight M_w: the higher the molecular weight is, the smaller is the pre-factor K_G. This implies that both factors, the mass-average molecular weight and the average number of entanglements per chain strongly affect the dependence of the shear modulus on strain rate.

Table 2 shows no direct correlations between the plateau modulus G_0 and the mass-average molecular weight M_w. It reveals, however, a noticeable dependence of G_0 on the ratio $M_\mathrm{w}/M_\mathrm{e}$: the larger the number of strands per chain is, the higher is the modulus G_0. This conclusion is in excellent agreement with the classical theory of rubber elasticity, which predicts that the elastic modulus is determined by the number of strands per unit volume, and it is independent of the average length of a strand.

According to Figure 3, the parameter A grows with strain-rate intensity, and the rate of increase in A with shear rate is practically independent of the network structure (the exponent $\nu_A \approx 0.4$ weakly depends on molecular weight and concentration of entanglements). Table 2 demonstrates, however, that the absolute values of A are noticeably affected by the ratio $M_\mathrm{w}/M_\mathrm{e}$: the coefficient K_A substantially decreases (by an order of magnitude) with average number of entanglements per chain. This finding seems natural if we recall that A (which is proportional to α) characterizes the influence of the network elasticity on the non-affine flow of junctions that is described by the tensor $\mathbf{M}$. When the number of junctions per unit volume is relatively large, stresses in strands are not sufficient to substantially affect the sliding process (which implies that $\mathbf{D}_\mathrm{s} \approx \beta\mathbf{D}$). On the contrary, for a network with a relatively small concentration of junctions, stresses in strands strongly influence flow of junctions (which means that the tensor $\mathbf{M}$ does not vanish, and, as a consequence, the coefficient α in Eq. (29) is relatively large).

According to Figure 4, the parameter b, that characterizes the rate of sliding of junctions driven by macro-deformation, grows with shear rate at all strain rates under consideration. For all solutions, the parameter b remains below unity. The rate of increase in b with $\dot{k}$

reaches maximum for PS2 (the lowest M_w), whereas these rates are rather modest for PS1 and PS3 (solutions with high molecular weights). Table 2 shows that the exponent ν_b in Eq. (44) increases with mass-average molecular weight, and it reveals no correlations with the average number of entanglements per chain.

According to Table 2, the coefficient r noticeably decreases with the ratio M_w/M_e. This implies that the effect of strain energy on the rate of internal dissipation [characterized by the coefficient α in Eq. (29)] is substantial for solutions of weakly entangled polymers and may be disregarded for strongly entangled networks.

9   Validation of the model

To verify the constitutive equations, we apply two approaches. According to the first, we analyze the same deformation mode (shear flow), but for a noticeably denser system and compare the conclusions drawn in the previous section with results of numerical simulation. Following the other approach, we focus on the response of a polymer melt at another deformation mode (extensional flow) and compare predictions of the governing equations (with the adjustable parameters found by fitting experimental data under simple shear) with observations.

1. We begin with the first approach and formulate explicitly some assertions that can be drawn for a dense polymer system from the analysis of results reported in Figures 3 to 5 and Table 2. As the network under consideration we chose LDPE melt (IUPAC A) whose physical properties are summarized in Table 1 with reference to [40, 41] (the mass-average molecular weight M_w and the number-average molecular weight M_n of the melt are given in [40]; to assess the average number of junctions along a chain, we use the graph depicted in Figure 3 of [41] and presume that the number of junctions exceeds the number of branching points for the highly branched LDPE melt). Our choice may be explained by two reasons. First, the observations in start-up shear tests on LDPE melt at the temperature $\Theta_0 = 150\,°C$ reported in [1] are accompanying by those in transient extensional tests on the same polymer at the same temperature [42], which allows results of numerical simulation to be compared at two different deformation modes. Secondly, these observations have recently been used to validate the pom–pom model [28]. Thus, the quality of fitting by the constitutive equations (42) and the pom–pom model may be collated on the same set of data.

The following hypotheses are introduced regarding the adjustable parameters of the melt:

(i) The modulus G should substantially exceed that for the solutions at all strain rates (this fact is not trivial because G is determined by fitting the entire dependencies of the shear stress on time). The coefficient G_0 should be relatively large, whereas the exponent ν_G in Eq. (43) should be rather small (these quantities are determined by the ratio M_w/M_e that is high for the melt). The pre-factor K_G in Eq. (43) should be relatively large (this quantity is inversely proportional to the mass-average molecular weight, while M_w of the melt is small compared with the molecular weights of PS solutions).

(ii) The coefficient r in Eq. (47) that describes the effect of strain energy on the rate of sliding of junctions should be relatively small (because the ratio M_w/M_e of the melt

exceeds that of PS solutions).

(iii) The exponent ν_A of the melt should be close to those of PS solutions (this parameter is independent of the molecular structure). The coefficient K_A in Eq. (46) that accounts for the influence of strain rate on the rate of sliding of junctions should be quite small (this quantity is inversely proportional to the average number of strands in a chain).

(iv) The exponent ν_b in Eq. (44) that describes the effect of strain rate on the parameter b (the latter characterizes the proportionality between the velocity gradients for macro-deformation and sliding of junctions) should be relatively small (because the ratio M_w/M_e of the melt exceeds that of PS solutions).

To examine these hypotheses, we begin with the approximation of the experimental data for the shear stress Σ_{12} plotted as a function of time in Figure 8. To reduce the number of material constants, we set $r = 0$ in accord with assumption (ii). To find the coefficients A, b and G, each curve $\Sigma_{12}(t)$ is fitted separately by using the same approach that was utilized in Section 7. We chose some values of A, b and G from the intervals $[0, A_{max}]$, $[0, b_{max}]$ and $[0, G_{max}]$, where the "best-fit" parameters are assumed to be located, integrate Eqs. (66) numerically, and calculate the shear stress Σ_{12} by means of Eq. (67). The "best-fit" coefficients A, b and G are found from the condition of minimum of the cost function R in Eq. (78), where the last term is disregarded.

Figure 8 demonstrates excellent agreement between the observations and the results of numerical simulation. It is worth noting that the quality of fitting the experimental data is noticeably higher than that for the pom–pom model with a substantially larger number of experimental constants, compare Figure 8 with Figure 9 in [28]. By no means, this conclusion implies that Eqs. (42) are superior with regard to the constitutive equations in the pom–pom model, as the latter are grounded on the solid basis of the molecular theory of polymer networks. We suppose that the good quality of matching observations with the smaller number of adjustable parameters revealed in Figure 8 may be explained by the fact that a detailed description of orientation and stretch of chains is excessive for the analysis of shear flows with relatively large strain rates.

The modulus G determined in the fitting procedure is plotted versus strain rate $\dot{k}$ in Figure 5. The dependence $G(\dot{k})$ is matched by Eq. (43) with the adjustable parameters G_0, K_G and ν_G reported in Table 2. Comparison of the results listed in Table 2 shows that the modulus G of the melt substantially exceeds that for the solutions (at least, by three orders of magnitude), the exponent ν_G for the melt is small compared to that for PS solutions, whereas the pre-factor K_G exceeds that for the solutions. All these conclusions are in perfect agreement with assumption (i).

It is obvious that assumption (ii) is fulfilled, as the value $r = 0$ was set in the fitting procedure.

The coefficient A is plotted versus $\dot{k}$ in Figure 3 together with its approximation by Eq. (79) with the coefficients K_A and ν_A listed in Table 2. Comparison of these parameters with appropriate parameters for PS solutions demonstrates that assumption (iii) is satisfied.

The parameter b is plotted versus strain-rate intensity D_i in Figure 4. This figure demonstrates that b is practically constant, which means that the exponent ν_b in Eq. (44) vanishes, in agreement with assumption (iv).

This analysis reveals that the approximation of experimental data in shear tests for polymer solutions by the constitutive model implies the assumptions regarding the behavior of material parameters of a melt that appear to be physically plausible.

2. To further examine the constitutive equations, we intend to deduce a relationship that does not contain adjustable parameters and that connects some quantities which may be measured directly in conventional tests. For this purpose, we confine ourselves to relatively dense polymer systems (melts), and, based on assertion (ii), set $r = 0$ in the governing equations. According to Eqs. (65) and (77), in this case the first normal stress function reads

$$\Psi_1 = \frac{2G(1-b)^3}{A^2} p_{20}^4. \tag{80}$$

Equations (76) and (80) result in

$$\frac{\Psi_1}{\eta_s} = \frac{2}{A}(1-b)p_{20}.$$

On the other hand, Eqs. (65) and (74) (where we set $r = 0$) imply that

$$\frac{1-b}{A} = \frac{1}{D_i}\sqrt{\frac{1-p_{20}^3}{p_{20}^5}}.$$

Combining these equalities, we find that

$$\frac{1-p_{20}^3}{p_{20}^3} = \left(\frac{\Psi_1 D_i}{2\eta_s}\right)^2,$$

which means that

$$p_{20} = \left[1 + \left(\frac{\Psi_1 D_i}{2\eta_s}\right)^2\right]^{-\frac{1}{3}}. \tag{81}$$

It follows from Eqs. (59) and (76) that

$$\eta_e = 3\eta_s p_{20}^{-3}.$$

Substituting expression (81) into this equality, we arrive at the formula

$$\eta_e = 3\eta_s\left[1 + \left(\frac{\Psi_1 D_i}{2\eta_s}\right)^2\right], \tag{82}$$

which expresses the steady elongational viscosity η_e in terms of the steady shear viscosity η_s and first normal stress function Ψ_1 for an arbitrary strain-rate intensity D_i.

To check the validity of Eq. (82), we use observations on polypropylene melt ($M_w = 3.5 \cdot 10^5$ g/mol) at $\Theta_0 = 190$ °C reported in Figure 10 of [37]. It should be noted that steady extensional and shear tests are conventionally performed at different strain rates, which implies that some results provided in [37] are extrapolations of experimental data. The steady elongational viscosity η_e is plotted versus strain-rate intensity D_i in Figure 9 (unfilled circles) together with its prediction by Eq. (82) (filled circles). For comparison, we also present the estimate of the elongational viscosity for a Newtonian fluid $\eta_e = 3\eta_s$

(asterisks). Figure 9 shows that Eq. (82) provides a reasonable correction of the Newtonian formula for the dependence of the elongational viscosity on strain rate.

To further examine Eq. (82), we consider experimental data for dilute solutions of polyacrylamide in water/glycerol solvent [43]. The observations depicted in Figures 4 and 6 of [43] show that the steady shear viscosity η_s and the first normal stress coefficient Ψ_1 remain practically constant at shear rates up to 200–500 s^{-1} (the low-shear plateau). Formula (82) predicts that in this region of strain rates, the steady elongational viscosity η_e should increase with strain-rate intensity (strain-thickening). This conclusion is in agreement with the data depicted in Figure 10 of [43], which show a pronounced increase (by an order of magnitude) in the elongational viscosity with $\dot\epsilon$ in the interval of strain rates from 1 to 200 s^{-1}. We do not provide qualitative comparison of the model predictions with these observations (as it was mentioned before, the assumption $r = 0$ is not necessary fulfilled for polymer solutions, whereas an analog of Eq. (82) for $r > 0$ becomes too cumbersome). However, it is worth noting that constitutive equations (42) can describe (at least, qualitatively) strain-thickening in polymer fluids. This conclusion is rather surprising, because the strain-thickening phenomenon is conventionally associated with coil-stretch transition in polymer solutions, while the latter effect is not accounted for by the model explicitly.

3. Our aim now is to show that Eqs. (42) can correctly describe the experimental data on elongational flows with constant strain rates (in particular, strain-hardening observed in uniaxial elongational tests) when their parameters are found by matching observations in shear tests. For this purpose, we study the evolution of the transient viscosity η_e^+ with time for the same LDPE melt that was used in the analysis of stress overshoot in shear tests. The experimental data in start-up elongational tests at $\Theta_0 = 150\,°C$ reported in [42] are depicted in Figure 10.

It is worth noting a pronounced difference between the observations in extensional and shear tests presented in Figures 8 and 10. While the stress overshoot and subsequent strain softening in shear tests (Figure 8) occur at times of the order of 1 to 10 s (at the chosen shear rates), a pronounced strain hardening is observed in extensional tests at times of the order of 10^{-2} to 10^{-1} s. In this time interval, our assumption regarding rapid tuning of the number of strands to its steady value corresponding to a given strain rate becomes inadequate, and the evolution of the function $N(t)$ should be taken into account.

Within the reptation concept, the quantity $N(t)$ equals the concentration of tubes survived until instant $t \geq 0$. It was demonstrated in [35] that changes in the number of survived tubes in a matrix of fixed obstacles are correctly described by a single-exponential function. This implies that, as a first approximation, the first-order kinetic equation can be introduced for the function $N(t)$,

$$\frac{dN}{dt}(t) = \frac{1}{\tau_r(D_i)}\Big[N^0(D_i) - N(t)\Big],$$

where $N^0(D_i)$ is the steady concentration of strands at deformation with the strain-rate intensity D_i, and $\tau_r(D_i)$ is the characteristic time for changes in the number of strands at transition from the rest to the steady flow. As the elastic modulus G is proportional to N, we find from this equation that the function $G(t)$ obeys the relation

$$\frac{dG}{dt}(t) = \frac{1}{\tau_r(D_i)}\Big[G^0(D_i) - G(t)\Big], \tag{83}$$

24

where $G^0(D_i)$ is given by Eq. (43).

After this correction of the governing equations driven by the necessity to account for the evolution of the elastic modulus, the transient viscosity η_e^+ in a start-up elongational test with a constant strain rate $\dot{\epsilon}$ is determined by Eq. (58), where the stress difference $\Delta\Sigma$ obeys Eq. (54), the function $\kappa(t)$ is governed by Eq. (53), and the coefficient G is described by Eq. (83).

The following procedure is applied to fit the observations at various strain rates $\dot{\epsilon}$ depicted in Figure 10. First, we set $r = 0$ and calculate $G^0(\dot{\epsilon})$ and $A(\dot{\epsilon})$ by using Eqs. (43) and (79) [where D_i is given by Eq. (52)] with the parameters G_0, K_G, ν_G, K_A and ν_A found in the approximation of observations in shear tests. As the initial condition G_{in} for Eq. (83) is unknown [it corresponds to the elastic modulus after sudden application of the external load and does not necessary coincide with G_0 in Eq. (43)], we begin with matching observations for the elongational viscosity in a test with the smallest strain rate $\dot{\epsilon} = 0.3$ s^{-1} (for this test, the largest number of experimental data are presented in Figure 10). The curve $\eta_e^+(t)$ is determined by 3 constants: G_{in}, b and τ_r (formally, the coefficient b found in the shear tests can be utilized, but we chose to treat b as an adjustable parameter in order to compare appropriate results in extensional and shear tests: the closeness of values of b found in two different tests will confirm that the fitting procedure is stable). The quantities G_{in}, b and τ_r are determined by the same algorithm that was employed in Section 7. We fix some intervals, where the "best-fit" parameters are located, divide these intervals into subintervals, for each triad chosen from the subintervals integrate Eqs. (53) and (83) numerically (by the Runge–Kutta method with the time-step $\Delta t = 1.0 \cdot 10^{-5}$ s), and calculate η_e^+ from Eqs. (54) and (58). The best-fit values of G_{in}, b and τ_r are chosen from the condition of minimum of the cost function

$$R = \sum_{t_m}\left[\eta_e^{\mathrm{exp}}(t_m) - \eta_e^{\mathrm{num}}(t_m)\right]^2,$$

where the sum is calculated over all experimental points t_m depicted in Figure 15, η_e^{exp} is the elongational viscosity measured in the test, and η_e^{num} is given by Eq. (58).

The initial modulus $G_{\mathrm{in}} \approx 2.0 \cdot 10^6$ Pa ensures the best approximation of the experimental data in the extensional test with the strain rate $\dot{\epsilon} = 0.3$ s^{-1}. We now fix this value and fit other curves depicted in Figure 10 by using the same algorithm with only two adjustable parameters, b and τ_r. Each set of observations is matched separately.

Figure 10 demonstrates quite reasonable agreement between the experimental data and the results of numerical simulation at all strain rates under consideration. The adjustable parameter b is plotted versus strain-rate intensity D_i in Figure 11. Comparison of the dependencies $b(D_i)$ found by matching observations in shear (unfilled circles) and extensional (filled circles) tests reveals that the experimental values of b practically coincide, which implies that the fitting algorithm is stable.

The parameter τ_r is plotted versus strain-rate intensity D_i in Figure 12 (unfilled circles). According to this figure, the parameter τ_r strongly decreases with strain-rate intensity D_i. The experimental data are approximated by the phenomenological relation

$$\log \tau_r = \tau_{r0} - \tau_{r1} \log D_i, \tag{84}$$

where the coefficients τ_{r0} and τ_{r1} are calculated by the least-squares method. Figure 12 shows that Eq. (84) ensures fair approximation of the observations. For comparison, we also

25

present in Figure 12 the instants τ_{p}, when the stress Σ_{12} in shear tests reaches its maximal values (filled circles). The observations are fitted by the formula similar to Eq. (84),

$$\log \tau_{\mathrm{p}} = \tau_{\mathrm{p}0} - \tau_{\mathrm{p}1} \log D_{\mathrm{i}} \qquad (85)$$

with the coefficients $\tau_{\mathrm{p}0}$ and $\tau_{\mathrm{p}1}$ found by the least-squares technique. Figure 12 demonstrates that at all strain rates under consideration, the peak instants τ_{p} substantially (at least, by an order of magnitude) exceed the relaxation times τ_{p}. This confirms our assumption that the evolution of the elastic modulus G with time can be disregarded in the analysis of stress overshoot under shear.

4. As the objective of this work is to study the rate-dependent behavior of polymer fluids at large deformations, we do not concentrate on their response in oscillatory tests with small strains and relaxation tests. It is instructive, however, to make some comments regarding the model predictions in conventional viscoelastic tests.

We begin with the analysis of governing equations at small strains. For this purpose, we set

$$\mathbf{B}_{\mathrm{e}} = \mathbf{I} + 2\hat{\epsilon}_{\mathrm{e}}, \qquad (86)$$

where $\hat{\epsilon}$ is the Finger strain tensor for elastic deformation, substitute expression (86) into Eqs. (42), and neglect terms of the second order of smallness with respect to $\hat{\epsilon}_{\mathrm{e}}$ and $\hat{\epsilon}$, where $\hat{\epsilon}$ is the strain tensor for macro-deformation. Using Eqs. (43) to (47), we arrive at the expression for the stress tensor,

$$\mathbf{\Sigma}(t) = -P(t)\mathbf{I} + 2G_0\hat{\epsilon}_{\mathrm{e}}(t), \qquad (87)$$

where the same notation P is employed for the unknown pressure. The evolution of the elastic strain tensor is described by the differential equation

$$\frac{d\hat{\epsilon}_{\mathrm{e}}}{dt}(t) + \frac{1}{\tau_{\mathrm{s}}}\hat{\epsilon}_{\mathrm{e}}(t) = \frac{d\hat{\epsilon}}{dt}(t), \qquad \tau_{\mathrm{s}} = \frac{1}{A_0}. \qquad (88)$$

Formulas (87) and (88) reveal that Eqs. (42) are transformed into the Maxwell model at small strains, which implies that these relations can adequately describe observations in conventional oscillatory tests, provided that the one-mode model (42) is replaced by its multi-mode analog. As this procedure is straightforward, we do not dwell on it in the present study.

Two comments are noteworthy. First, the fact that the elastic modulus at small strains coincides with G_0 provides an additional opportunity to verify the model predictions, because G_0 can be measured independently in shear relaxation tests, on the one hand, and it can be calculated from Eq. (43) by fitting the experimental data on $G(\dot{k})$ in start-up shear tests, on the other. Although we do not expect this procedure to result in the same values of G_0 for LDPE melt [we have only 4 data points for $G(\dot{k})$ that are approximated by the three-parameter formula (43), which means that the accuracy of determining G_0 is rather poor], we would mention that the value $G_0^{\mathrm{start-up}} = 6.5 \cdot 10^4$ Pa reported in Table 2 overestimates by less than twice the value $G_0^{\mathrm{rel}} = 3.4 \cdot 10^4$ Pa evaluated from the data in relaxation tests with small strains [1].

Secondly, the relaxation time τ_{s} in Eq. (88) is inversely proportional to the parameter A_0. To derive constitutive equations that are equivalent to the Maxwell model at small

strains was the main reason to preserve the first term in phenomenological equation (46) despite the fact that all observations in the interval of strain rates under consideration can be approximated quite well by Eq. (79) without A_0. Following Eq. (88), we can introduce an effective relaxation time τ_s for an arbitrary strain-rate intensity G_i as the reciprocate of the function $A(D_i)$. The experimental data for $\tau_s(D_i)$ are depicted in Figure 12 together with their approximation by the equation analogous to Eqs. (84) and (85),

$$\log \tau_s = \tau_{s0} - \tau_{s1} \log D_i. \tag{89}$$

The coefficients τ_{s0} and τ_{s1} in Eq. (89) are found by the least-squares technique. Figure 12 shows that the slopes of the curves $\tau_r(D_i)$ and $\tau_s(D_i)$ are quite similar, and for all strain rates, the effective relaxation time τ_s exceeds the relaxation time for the elastic modulus τ_r by two orders of magnitude. This provides another confirmation of our hypothesis that the evolution of the elastic modulus G to its ultimate value $G^0(D_i)$ may be neglected in the study of start-up tests. Figure 12 also shows that given a strain rate, the effective relaxation time τ_s is substantially higher than the time for stress overshoot τ_p, which means that τ_p cannot be employed to assess the function $A(D_i)$, and the entire curves $\Sigma_{12}(t)$ should be approximated to determined the model parameters.

Finally, we consider relaxation tests with finite deformations. In these experiments, constitutive equations (42) with necessary correction (83) demonstrate a time-dependent behavior with two characteristic time-scales: (i) rapid relaxation driven by changes in the modulus G and (ii) slow decrease in stress associated with the Maxwell-type evolution of the elastic Cauchy–Green tensor $\mathbf{B}_e$ in Eqs. (42). This implies that the stress in a step-strain test cannot be factorable into a product of a strain-dependent and time-dependent functions. As the same features are also revealed by the pom–pom model, we do not discuss them in detail, referring to [31], where recent observations data are analyzed that confirm the presence of two time-scales in the viscoelastic response of polymer fluids.

10 Concluding remarks

A constitutive model has been developed for a polymer fluid. A polymer is thought of as an incompressible network of strands bridged by junctions. The network is treated as permanent (strands cannot separate from their nodes). The junctions between strands can slide with respect to their reference positions under deformation. No restrictions are imposed on the rate-of-strain tensor for sliding of junctions, whereas the vorticity tensor for sliding is proportional to that for macro-deformation. Stress–strain relations are derived by using the laws of thermodynamics. For a Gaussian network of strands, the constitutive equations involve three adjustable functions, for which phenomenological relations are introduced.

In a broad sense, the constitutive equations may be treated as a combination of the Johnson–Segalman and Leonov models. The important advantages of these relations are that (i) they are based on the conventional multiplicative decomposition of the deformation gradient (no slip tensors are used), and (ii) they presume (in agreement with the classical theories in polymer physics) the strain energy of strands to be Gaussian (no complicated formulas are introduced for the elastic energy).

The governing equations are simplified for uniaxial extension and simple shear with finite strains. Explicit formulas are developed for the steady elongational and shear viscosities, as well as for the normal stress functions.

To verify the model, three sets of experimental data are approximated for monodisperse polystyrene solutions with various molecular weights and molecular weights between entanglements. Good agreement is demonstrated between the observations for stress overshoot in start-up shear tests and the results of numerical simulation at various strain rates. It is revealed that the phenomenological relations correctly characterize the effect of strain rate on the material parameters, and their coefficients change consistently with mass-average molecular weight and concentration of entanglements.

To validate the governing equations, the evolution of stresses is studied in start-up extensional and shear flows on low-density polyethylene melt. It is demonstrated that constitutive equations (42) and (83) adequately describe changes in the elongation viscosity with time when their parameters are found by matching observations in shear tests.

Our approximation of observations in extensional and shear flows of LDPE melt demonstrates higher quality of fitting compared to the pom–pom model. An advantage of constitutive equations (42) is that they can also be used to match the experimental data on dilute polymer solutions, a class of polymer fluids to which the pom–pom model is inapplicable.

New formula (82) has been derived that expresses the steady elongational viscosity in terms of the steady shear viscosity and the first normal stress function. The validity of this equation is confirmed by observations on polypropylene melt.

The following characteristic features of the constitutive equations have been revealed:

1. The model can quantitatively describe overshoots for the shear stress and the first normal stress difference in polymer melts and solutions, as well as stress undershoot in polymer solutions.

2. It can quantitatively describe strain hardening in start-up extensional tests.

3. The governing equations can qualitatively predict strain-thickening in steady extensional tests.

4. The model can qualitatively describe two-scale stress relaxation in polymer fluids in step-strain tests.

5. At small strains, the constitutive equations are transformed into the conventional Maxwell model.

References

[1] J. Meissner, Modifications of the Weissenberg rheogoniometer for measurements of transient rheological properties of molten polyethylene under shear. Comparison with tensile data, J. Appl. Polym. Sci. 16 (1972) 2877.

[2] M.H. Wagner, Analysis of time-dependent non-linear stress-growth data for shear and elongational flow of a low-density branched polyethylene melt, Rheol. Acta 15 (1976) 136.

[3] M.C. Phillips, The prediction of time-dependent non-linear stresses in viscoelastic materials. 2. Prediction of shear and uniaxial elongation behavior, J. Non-Newtonian Fluid Mech. 2 (1977) 123.

[4] H.H. Saab, R.B. Bird and C.F. Curtiss, A kinetic theory for polymer melts. 5. Experimental comparisons for shear-flow rheological properties, J. Chem. Phys. 77 (1982) 4758.

[5] P. Rubio and M.H. Wagner, LDPE melt rheology and the pom-pom model, J. Non-Newtonian Fluid Mech. 92 (2000) 245.

[6] P.G. Santangelo and C.M. Roland, Interrupted shear flow of unentangled polystyrene melts, J. Rheol. 45 (2001) 583.

[7] C. Lacroix, M. Grmela and P.J. Carreau, Relationships between rheology and morphology for immiscible molten blends of polypropylene and ethylene copolymers under shear flow, J. Rheol. 42 (1998) 41.

[8] R.E.S. Bretas and R.L. Powell, Dynamic and transient rheological properties of glass-filled polymer melts, Rheol. Acta 24 (1985) 69.

[9] M.J. Solomon, A.S. Almusallam, K.F. Seefeldt, A. Somwangthanaroj and P. Varadan, Rheology of polypropylene/clay hybrid materials, Macromolecules 34 (2001) 1864.

[10] A.D. Drozdov, Finite viscoplasticity of non-affine networks: stress overshoot under shear, Continuum Mech. Thermodyn. 16 (2004) 73.

[11] J.P. Oberhauser, L.G. Leal and D.W. Mead, The response of entangled polymer solutions to step changes of shear rate: signatures of segmental stretch? J. Polym. Sci. Part B: Polym. Phys. 36 (1998) 265.

[12] K. Osaki, T. Inoue and T. Isomura, Stress overshoot of polymer solutions at high rates of shear, J. Polym. Sci. Part B: Polym. Phys. 38 (2000) 1917.

[13] K. Osaki, T. Inoue and T. Isomura, Stress overshoot of polymer solutions at high rates of shear; polystyrene with bimodal molecular weight distribution, J. Polym. Sci. Part B: Polym. Phys. 38 (2000) 2043.

[14] R. Klucker, F. Candau and F. Schosseler, Transient behavior of associating copolymers in a shear flow, Macromolecules 28 (1995) 6416.

[15] P. Fischer and H. Rehage, Non-linear flow properties of viscoelastic surfactant solutions, Rheol. Acta 36 (1997) 13.

[16] J.F. Berret, Transient rheology of wormlike micelles, Langmuir 13 (1997) 2227.

[17] S. Lerouge, J.P. Decruppe and C. Humbert, Shear banding in a micellar solution under transient flow, Phys. Rev. Lett. 81 (1998) 5457.

[18] C.D. Han, V.M. Ugaz and W.R. Burghardt, Shear stress overshoots in flow inception of semiflexible thermotropic liquid crystalline polymers: experimental test of a parameter-free model prediction, Macromolecules 34 (2001) 3642.

[19] D. Grecov and A.D. Rey, Transient rheology of discotic mesophases, Rheol. Acta 42 (2003) 590.

[20] K. Krishnan, W.R. Burghardt, T.P. Lodge and F.S. Bates, Transient rheology of a polymeric bicontinuous microemulsion, Langmuir 18 (2002) 9676.

[21] F. Yziquel, P.J. Carreau, M. Moan and P.A. Tanguy, Rheological modeling of concentrated colloidal suspensions, J. Non-Newtonian Fluid Mech. 86 (1999) 133.

[22] A. Mujumdar, A.N. Beris and A.B. Metzner, Transient phenomena in thixotropic systems, J. Non-Newtonian Fluid Mech. 102 (2002) 157.

[23] W. Stasiak and C. Cohen, Multiple-time scale approach to stress growth in suspensions of rodlike macromolecules, J. Non-Newtonian Fluid Mech. 25 (1987) 277.

[24] H. Giesekus, A simple constitutive equation for polymer fluids based on the concept of deformation-dependent tensorial mobility, J. Non-Newtonian Fluid Mech. 11 (1982) 69.

[25] F. Tanaka and S.F. Edwards, Viscoelastic properties of physically cross-linked networks. Transient network theory, Macromolecules 25 (1992) 1516.

[26] K.R. Geurts and L.E. Wedgewood, A finitely extensible network strand model with nonlinear backbone forces and entanglement kinetics, J. Chem. Phys. 106 (1997) 339.

[27] C.C. Hua, J.D. Schieber and D.C. Venerus, Segment connectivity, chain-length breathing, segmental stretch, and constraint release in reptation models. 3. Shear flows, J. Rheol. 43 (1999) 701.

[28] R.J.Blackwell, T.C.B. McLeish and O.G. Harlen, Molecular drag–strain coupling in branched polymer melts, J. Rheol. 44 (2000) 121.

[29] C. Pattamaprom and R.G. Larson, Constraint release effects in monodisperse and bidisperse polystyrenes in fast transient shearing flows, Macromolecules 34 (2001) 5229.

[30] J.D. Schieber, Internal viscosity dumbbell model with a Gaussian approximation, J. Rheol. 37 (1993) 1003.

[31] T.C.B. McLeish and R.G. Larson, Molecular constitutive equations for a class of branched polymers: The pom–pom model, J. Rheol. 42 (1998) 81.

[32] M.W. Johnson and D. Segalman, A model for viscoelastic fluid behavior which allows non-affine deformation, J. Non-Newtonian Fluid Mech. 2 (1977) 255.

[33] N. Phan Thien and R.I. Tanner, A new constitutive equation derived from network theory, J. Non-Newtonian Fluid Mech. 2 (1977) 353.

[34] M. Simhambhatla and A.I. Leonov, On the rheological modeling of viscoelastic polymer liquids with stable constitutive equations, Rheol. Acta 34 (1995) 259.

[35] M. Doi and S.F. Edwards, The theory of polymer dynamics, Oxford University Press: Oxford, 1986.

[36] J. Des Cloizeaux, Double reptation vs simple reptation in polymer melts, Europhys. Lett. 5 (1988) 437.

[37] G. Barakos, E. Mitsoulis, C. Tzoganakis and T. Kajiwara, Rheological characterization of controlled-rheology polypropylenes using integral constitutive equations, J. Appl. Polym. Sci. 59 (1996) 543.

[38] T. Schweizer, Measurement of the first and second normal stress differences in a polystyrene melt with a cone and partitioned plate tool, Rheol. Acta 41 (2002) 337.

[39] S.E. Mall-Gleissle, W. Gleissle, G.H. McKinley and H. Buggisch, The normal stress behaviour of suspensions with viscoelastic matrix fluids, Rheol. Acta 41 (2002) 61.

[40] J.H. Magill, S.V. Peddada and G.M. McManus, Crystallization–morphology–polymer processing correlations for IUPAC low density polyethylenes. Polym. Eng. Sci. 21 (1981) 1.

[41] P.D. Iedema, M. Wulkow and H.C.J. Hoefsloot, Modeling molecular weight and degree of branching distribution of low-density polyethylene. Macromolecules 33 (2000) 7173.

[42] H. Münstedt and H.M. Laun, Elongational behaviour of a low density polyethylene melt II, Rheol. Acta 18 (1979) 492.

[43] E. Pelletier, C. Viebke, J. Meadows and P.A. Williams, Dilute polyacrylamide solutions under uniaxial extensional flow. Langmuir 19 (2003) 559.

List of tables

Table 1: Concentrations c, mass-average molecular weights M_w, polydispersity indices D, and average numbers of entanglements per chain $M_\mathrm{w}/M_\mathrm{e}$ for PS solutions and LDPE melt

Abbreviation	c	M_w g/mol	D	$M_\mathrm{w}/M_\mathrm{e}$	Reference
PS1	3.0 wt-%	$8.42 \cdot 10^6$	1.17	10.0	[11]
PS2	0.1 g/cm^3	$1.09 \cdot 10^6$		6.1	[12]
PS3	0.1 g/cm^3	$8.24 \cdot 10^6$		1.8	[13]
LDPE		$2.47 \cdot 10^5$	15.2	over 60	[40, 41]

Table 2: Adjustable parameters for LDPE melt and PS solutions

Abbreviation	$\log K_A$	ν_A	$\log K_b$	ν_b	G_0 Pa	K_G	ν_G	r
LDPE	-1.09	0.40	-0.06	0.0	$6.5 \cdot 10^4$	0.172	0.11	0.0
PS1	-0.77	0.40	-0.75	0.0	79.7	0.058	0.34	0.1
PS2	-0.37	0.31	-0.78	0.60	59.6	0.144	0.51	0.2
PS3	-0.15	0.37	-0.32	0.15	22.0	0.082	0.91	0.4

List of figures

Figure 1: The shear stress Σ_{12} versus time t. Symbols: experimental data on PS1 in shear tests with the strain rates $\dot{k} = 4.0$ (unfilled circles), 2.0 (filled circles), 1.0 (asterisks), 0.5 (stars) and 0.2 s^{-1} (diamonds) [11]. Solid lines: results of numerical simulation.

Figure 2: The first normal stress difference N_1^+ versus time t. Symbols: experimental data on PS1 in shear tests with the strain rates $\dot{k} = 4.0$ (unfilled circles), 2.0 (filled circles), 1.0 (asterisks), 0.5 (stars) and 0.2 s^{-1} (diamonds) [11]. Solid lines: results of numerical simulation.

Figure 3: The parameter A versus shear rate $\dot{k}$. Symbols: treatment of observations on solutions PS1 (unfilled circles), PS2 (filled circles), PS3 (asterisks), and LDPE melt (diamonds). Solid lines: approximation of the experimental data by Eq. (79).

Figure 4: The dimensionless parameter b versus shear rate $\dot{k}$. Symbols: treatment of observations on solutions PS1 (unfilled circles), PS2 (filled circles), PS3 (asterisks), and LDPE melt (diamonds). Solid lines: approximation of the experimental data by Eq. (79).

Figure 5: The elastic modulus G versus shear rate $\dot{k}$. Symbols: treatment of observations on solutions PS1 (unfilled circles), PS2 (filled circles), PS3 (asterisks), and LDPE melt (diamonds). Solid lines: approximation of the experimental data by Eq. (43).

Figure 6: The shear stress Σ_{12} versus time t. Circles: experimental data on PS2 in shear tests with the strain rates $\dot{k} = 5.8$ (unfilled circles), 2.9 (filled circles), 1.74 (asterisks), 1.0 (stars), 0.63 (diamonds), 0.4 (triangles) and 0.1 s^{-1} (daggers) [12]. Solid lines: results of numerical simulation.

Figure 7: The shear stress Σ_{12} versus time t. Symbols: experimental data on PS3 in shear tests with the strain rates $\dot{k} = 7.77$ (unfilled circles), 5.55 (filled circles), 2.78 (asterisks), 2.24 (stars) and 1.39 s^{-1} (diamonds) [13]. Solid lines: results of numerical simulation.

Figure 8: The shear stress Σ_{12} versus time t. Symbols: experimental data on LDPE melt in shear tests with the strain rates $\dot{k} = 10.0$ (unfilled circles), 5.0 (filled circles), 2.0 (asterisks), and 1.0 s^{-1} (stars) [1]. Solid lines: results of numerical simulation.

Figure 9: The steady elongational viscosity η_e versus strain-rate intensity D_i. Unfilled circles: experimental data on polypropylene melt in uniaxial extensional tests [37]. Filled circles: predictions of Eq. (82). Asterisks: the Newtonian estimate $\eta_e = 3\eta_s$.

Figure 10: The transient elongational viscosity η_e^+ versus time t. Symbols: experimental data on LDPE melt in uniaxial extensional tests with the strain rates $\dot{\epsilon} = 0.3$ (unfilled circles), 1.0 (filled circles), 3.0 (asterisks), 10.0 (stars) and 30 s^{-1} (diamonds) [42]. Solid lines: results of numerical simulation.

Figure 11: The dimensionless parameter b versus strain-rate intensity D_i. Symbols: treatment of observations on LDPE melt in shear (unfilled circles) and extensional (filled circles) tests. Solid line: approximation of the experimental data by the constant $b = 0.85$.

Figure 12: The relaxation time for the elastic modulus $\tau = \tau_{\mathrm{r}}$ (unfilled circles), the time for stress overshoot $\tau = \tau_{\mathrm{p}}$ (filled circles) and the effective relaxation time for sliding of junctions $\tau = \tau_{\mathrm{s}}$ (asterisks) versus strain-rate intensity D_{i}. Symbols: treatment of observations on LDPE melt in shear and extensional tests. Solid lines: approximation of the experimental data by Eqs. (84), (85) and (89) with $\tau_{\mathrm{r}0} = -0.88$, $\tau_{\mathrm{r}1} = 0.48$, $\tau_{\mathrm{p}0} = 0.47$, $\tau_{\mathrm{p}1} = 0.62$, and $\tau_{\mathrm{s}0} = 0.40$, $\tau_{\mathrm{s}1} = 1.09$.
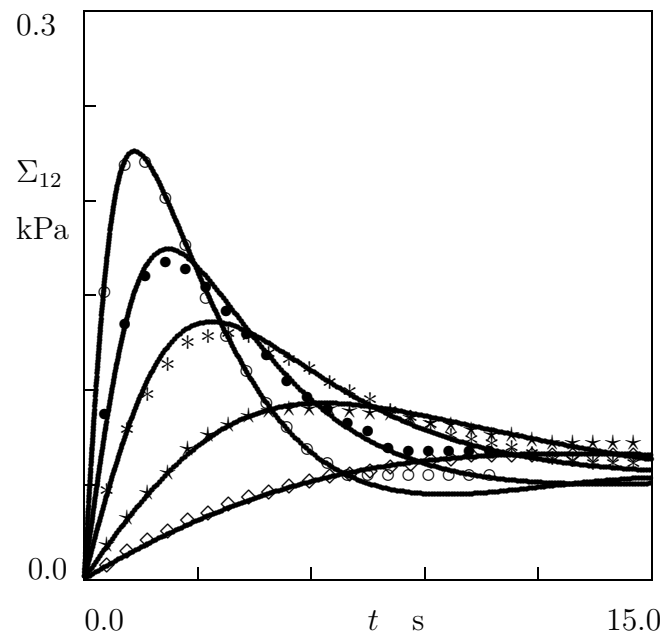
Figure 1:
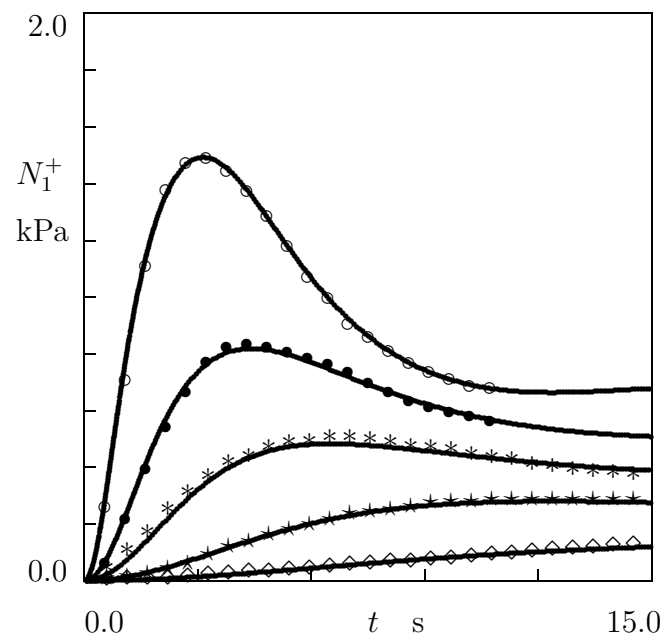
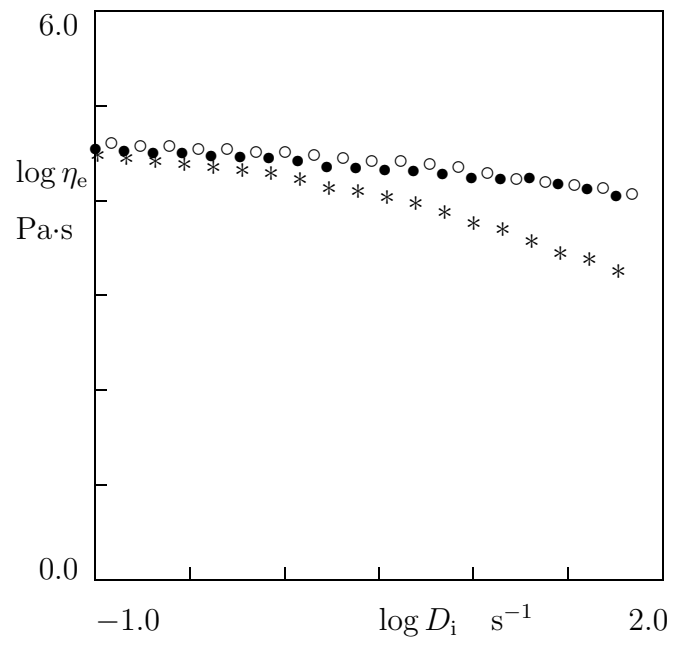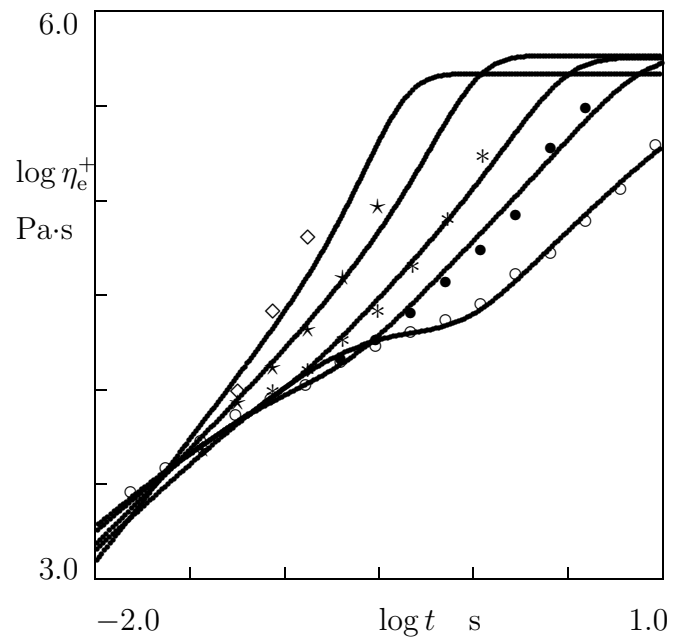

Figure 2:
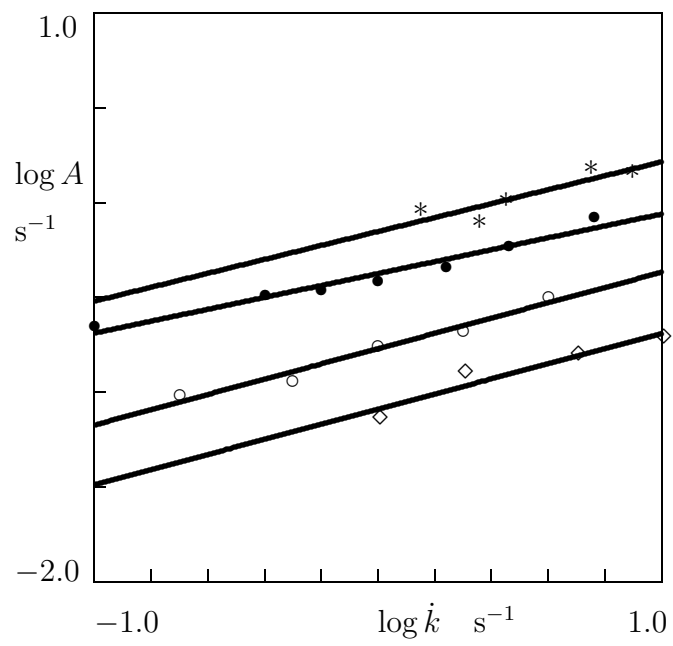
Figure 3:
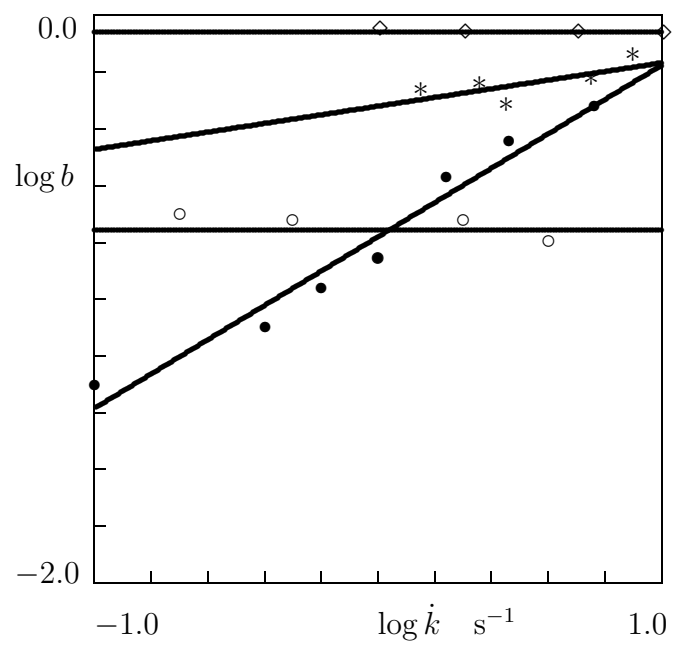
Figure 4:
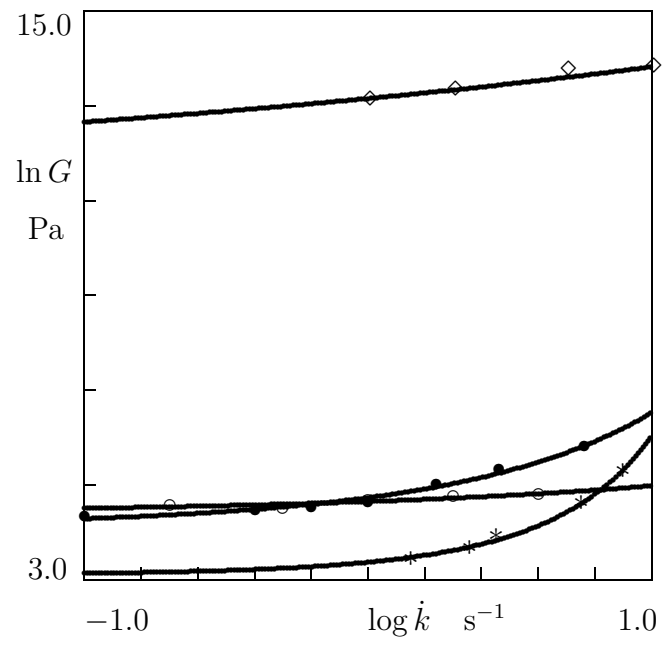
Figure 5:
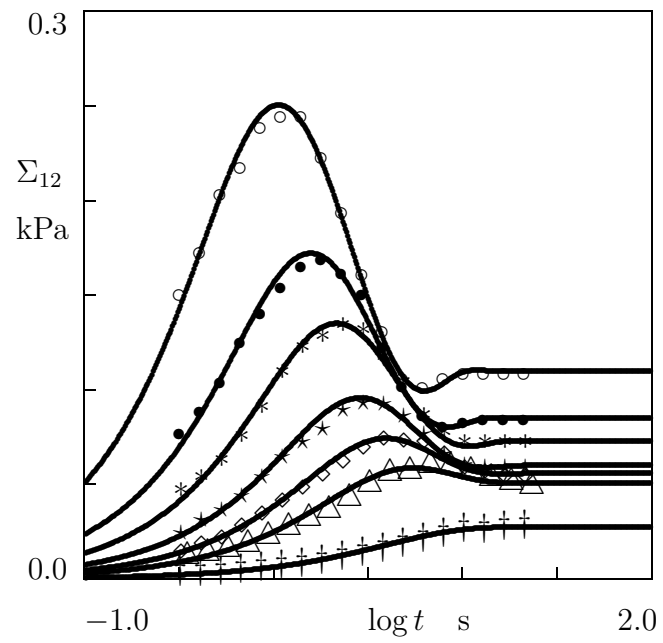
Figure 6:
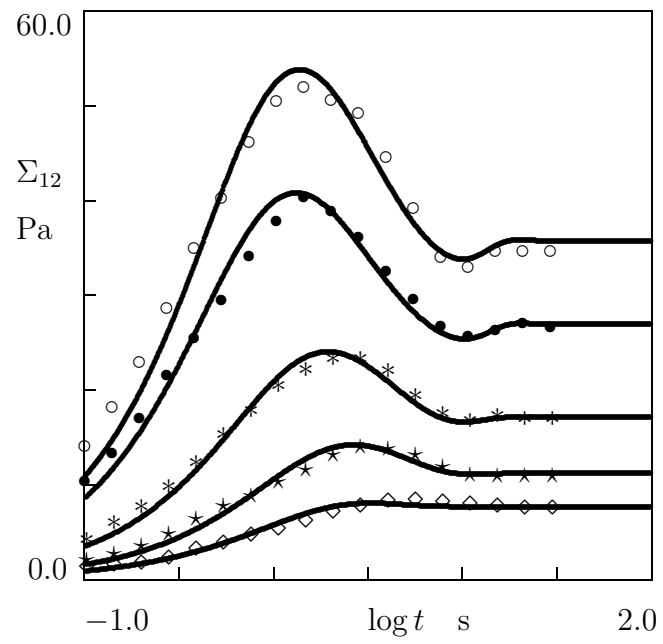
Figure 7:
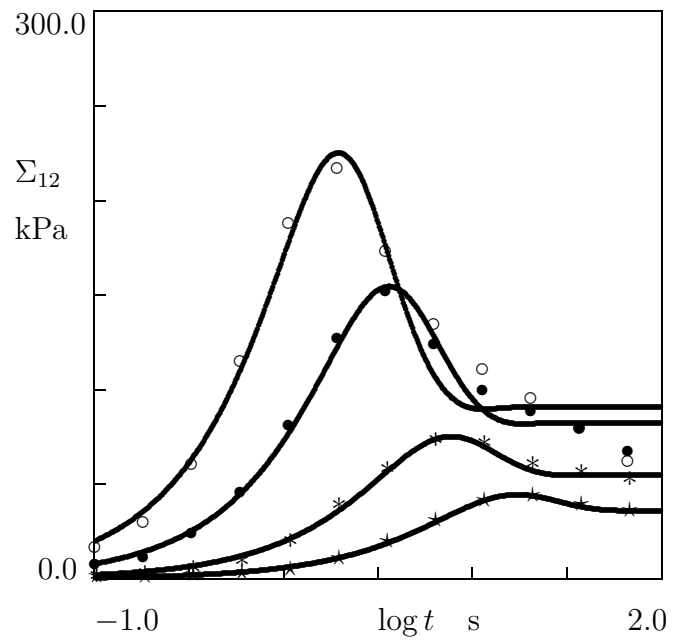
Figure 8:

Figure 9:

Figure 10:

Figure 11:

Figure 12: